bioRxiv preprint doi: https://doi.org/10.1101/2020.12.08.415687; this version posted December 8, 2020. The copyright holder for this preprint (which was not certified by peer review) is the author/funder, who has granted bioRxiv a license to display the preprint in perpetuity. It is made available under aCC-BY-NC-ND 4.0 International license.

Cryo-EM structures of outer-arm dynein array bound to microtubule doublet reveal a mechanism for motor coordination

Qinhui Rao[1], Yue Wang[1,*], Pengxin Chai[1,*], Yin-Wei Kuo[1], Long Han[1], Renbin Yang[1], Yuchen Yang[1], Jonathon Howard[1], and Kai Zhang[1,]**

[1]Department of Molecular Biophysics and Biochemistry, Yale University, New Haven, CT, 06511, USA
[*]These authors contributed equally to this work.
[**]Correspondence author. Email: jack.zhang@yale.edu

Thousands of outer-arm dyneins (OADs) are arrayed in the axoneme to drive a rhythmic ciliary beat. Using electron microscopy, we determined the structure of OAD array bound to microtubule doublets (MTDs) in near-atomic details and illuminate how OADs coordinate with each other to move one step forward. OAD prefers a specific pattern of MTD protofilaments for its distinct microtubule-binding domains. Upon MTD binding, free OADs are induced to adopt a stable parallel conformation, primed for array formation. Extensive tail-to-head (TTH) interactions between OADs are observed, which need to be broken for ATP turnover by the dynein motor. ATP-hydrolysis in turn relaxes the TTH interfaces to sequentially effectuate free nucleotide cycle of downstream OADs. These findings lead to a model for how conformational changes of OADs produce coordinated actions.

Motile cilia are evolutionarily conserved organelles that drive the movement of individual cells or transport extracellular fluids. Outer-arm dynein (OAD) is the key motor protein that generates the majority of mechanical forces required for ciliary beating *(1, 2)*. In a typical '9 + 2' cilium (Fig. 1A), thousands of OAD molecules are assembled onto the axonemal microtubule doublets (MTDs) as ordered arrays. Defects of OAD arrays in human lead to diseases, particularly the primary ciliary dyskinesia (PCD) *(3–5)*. To accomplish a rhythmic and energy-efficient beat, it is thought to be essential that OADs in the axoneme coordinate with each other. The regulation of ciliary beat involves various factors, including many different axonemal components, extracellular signals, and local geometry changes *(2)*. Nevertheless, lacking a deep understanding of the structural basis for OAD array formation and conformational coordination between OADs has been a major barrier to unveiling the mechanism of ciliary beat and its implications in human diseases.

We purified native OAD and MTD from *T. thermophila* and reconstituted the isolated OAD onto MTD (OAD-MTD) *(6)* for biochemical and cryo-EM analysis (figs. S1 and S2, and table S1). Microtubule-gliding assays indicated that the isolated OADs are active in vitro (Fig. 1B). The gliding velocity is positively correlated with the OAD concentration as well as microtubule length (fig. S1, B and C) *(7)*. Evidence from a previous study showed that the microtubule sliding is strikingly fast if OADs are aligned in bundles *(8)*. Besides, our reconstitution assay reveals that ordered OAD arrays can be spontaneously formed in the presence of MTD, in line with a previous finding *(6)*. These together suggest that multiple OADs tend to unify their forces to slide microtubules. To elucidate how OADs coordinate their actions, we performed cryo-EM on both free OAD and reconstituted OAD arrays. Free OADs are extremely flexible and do not have a stable conformation (fig. S1, D and E). We managed to obtain a structure of free OAD in a notable pre-parallel state at 5-12 Å resolutions in different regions (fig. S1, F to H). The OAD arrays adopt two distinct microtubule-binding states (MTBS-1 and MTBS-2) (fig. S2, D and E), which agrees with our observation by cryo-electron tomography (fig. S2, F and G). OAD unit together with the four binding protofilaments (OAD-PF) were locally refined to 2.8-3.8 Å resolutions for most regions in MTBS-1 and 3.8-6 Å resolutions in MTBS-2 (Fig. 1, C and D, figs. S3 to S6). Together with mass spectrometry and a genome-wide pattern search, eighteen unique subunits of OAD were unambiguously identified, built and refined (Fig. 1E, and tables S2 and S3).

The arrayed OADs adopt a fully parallel conformation (Fig. 1C) and fit well into in-situ cryo-ET maps (fig. S7, A to C) *(9, 11–13)*, indicating that our reconstituted arrays reflect the native structures in cilia. Compared to the dynamic OAD in the free form, the parallel OAD has a characteristic conformation with the motor domains stacked together. The stacking is mediated by interactions between dynein linkers (Linkers) and AAA+ rings (Rings) [referred to as Linker-Ring (LR) interactions] (fig. S7, D and E). Our cryo-EM reconstruction reveals there are four subunits that form the core structure of OAD (core-OAD), including two heavy chains (α- and β-HC) and two intermediate chains (IC2 and IC3). The core-OAD is conserved across species and all the four subunits are critical for OAD assembly *(1)*. They together serve as a scaffold for binding all other chains and mediate nearly all interactions between two adjacent OADs via a 'tail-to-head' (TTH) manner (Fig. 1, C and D). Apart from the core, the complete OAD from *T. thermophila* contains a special γ-HC and thirteen LCs (Fig. 1E, figs. S8 and S9) for regulatory roles *(14–19)*. γ-HC extends out from the core-OAD array with its N-terminal kelch domain (γ-kelch) tightly bound to the helical bundle 6 (HB6) of β-tail (fig. S8, A and B). Following the γ-kelch are two consecutive immunoglobulin folds, Ig-PT and Ig-Fln (fig. S8C)

bioRxiv preprint doi: https://doi.org/10.1101/2020.12.08.415687; this version posted December 8, 2020. The copyright holder for this preprint (which was not certified by peer review) is the author/funder, who has granted bioRxiv a license to display the preprint in perpetuity. It is made available under aCC-BY-NC-ND 4.0 International license.

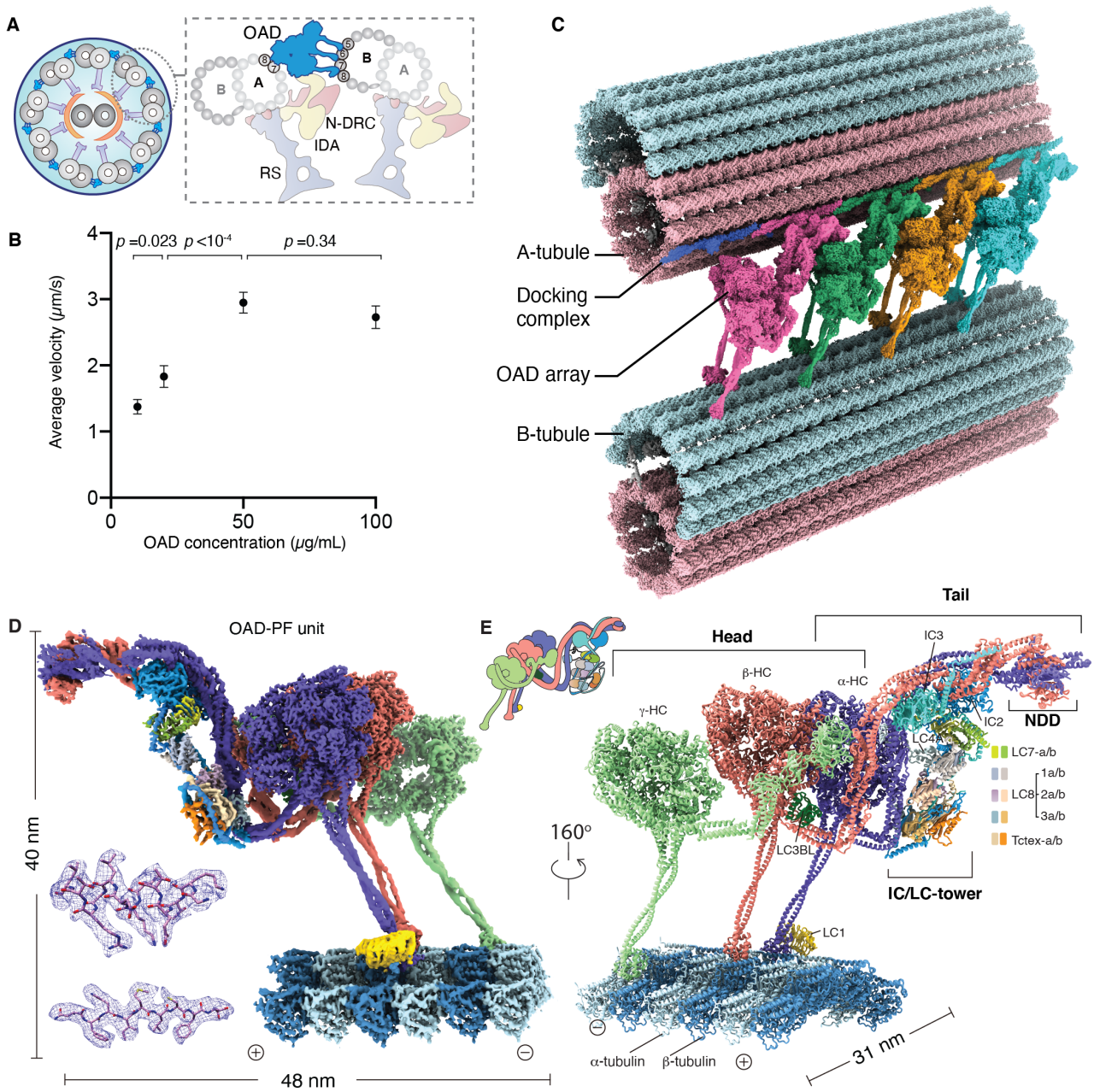

Fig. 1. Overall structure of OAD array bound to MTD. (A) Diagrams of the *T. thermophila* cilium and OAD bound to two adjacent MTDs. **(B)** The mean velocities of microtubule gliding by different concentrations of free OAD. **(C)** The side view of the cryo-EM structure of OAD array bound to two adjacent MTDs. The map is generated by fitting our cryo-EM maps of OAD array and MTDs into a previously reported cryo-ET reconstruction of the *T. thermophila* axoneme (EMD-7805) *(9)* as well as our own cryo-ET map. Model of the docking complex was based on *C. reinhardtii* homologue (PDB-6U42) *(10)*. **(D)** Density map of one OAD-PF unit in MTBS-1. The map was a combination of 31 locally refined regions. **(E)** A molecular model of the OAD-PF structure built from the map in **(D)**. Names of LC7, LC8 and Tctex are based on their relative positions, 'b' for those facing microtubule minus-end and 'a' for the opposite.

(1, 20). In contrast to the classical unprimed cytoplasmic dyneins [post-powerstroke state 1 (Post-1)] *(21–23)* as well as OAD α- and β-HC in MTBS-1, the γ-HC adopts a distinct state [post-powerstroke state 2 (Post-2)] with its Linker upraised toward AAA3-4 (fig. S8D). Among all the thirteen light chains (LCs), ten (LC7, LC8, and Tctex families) are clustered by the IC2/3 N-terminal extensions (NTEs). They together form a tower-like structure (IC/LC-tower) (Fig. 1E and fig. S9A) and attach to α-tail en bloc, facing toward the inner side of axoneme. Each position of the tower is occupied by a unique LC for its specific surrounding interfaces (fig. S9B). Attributed to a special helical bar and a beta-hairpin of IC2, the Tctex dimer is folded back and pinned to LC8s, linking the IC/LC-tower to either N-DRC or IADs in the axoneme (fig. S9D). With more than ten different proteins interwoven, this local region is tightly attached to the HB8 of α-neck and is likely to mediate the communication between inner axonemal components and OAD array. The other three LCs include an LC3B-like subunit (LC3BL, thioredoxin) which contacts Ig-PT and links the γ-tail to β-Linker (fig. S8C), LC4A (calmodulin) which binds to α-HB6 and links α-tail to IC/LC-tower (fig. S9E), and LC1 bound to

bioRxiv preprint doi: https://doi.org/10.1101/2020.12.08.415687; this version posted December 8, 2020. The copyright holder for this preprint (which was not certified by peer review) is the author/funder, who has granted bioRxiv a license to display the preprint in perpetuity. It is made available under aCC-BY-NC-ND 4.0 International license.

microtubule-binding domain of α-HC (α-MTBD) (Fig. 1, D and E).

Different from cytoplasmic dynein-1 which requires dynactin to align the two motor domains *(7, 24)*, the parallel OAD conformation is spontaneously induced by microtubule binding (figs. S1C and S2B), which triggers formation of an ordered OAD array. Cryo-EM classification indicated that OAD units along each array are locally synchronized and have the same microtubule-binding state (fig. S10A). However, the relative rotations between each two adjacent protofilaments [inter-PF angles *(25)*] vary significantly around the MTD surface (fig. S10, B and C). To preserve a stable parallel architecture, the OAD stalks need to rotate with respect to the MTBD regions to compensate for the inter-PF angles. This is enabled by the hinges between stalk coiled-coil helix 1 and MTBD helix 1 (CC1-H1) (Fig. 2A, and fig. S10, B and C). We compared the inter-PF angles from our OAD-PF reconstruction with that of the native B5-B8 PFs. The overall patterns strikingly match each other (a drop of inter-PF angle in B6-B7 and an increase in B7-B8) (Fig. 2B) *(25, 26)*, implying a preferred inter-PF pattern. Our cryo-EM reconstruction reveals that the pattern preference is attributed to the three distinctive MTBDs. The α-MTBD specifically binds the conserved LC1 with its helix H5 (Fig. 2A, and fig. S10D) *(18)*. The α-MTBD/LC1 complex requires a wider inter-PF space (similar to that between B7 and B8) to properly interact with adjacent tubulins (Fig. 2B). This is mediated by a cluster of positively charged residues *(27)* on the LC1 surface that attracts the C-terminal tail of β-tubulin (β-CTT) from an adjacent PF (fig. S10D). Meanwhile, LC1-binding forces the flap of α-MTBD to fit a conformation without contacting β-CTT. By contrast, the γ-flap directly contacts β-CTT (fig. S10E). The β-MTBD has a much shorter flap (fig. S10F) and lacks density connection with β-CTT, similar to that in dynein-1 *(28)*. These features collectively facilitate the landing of OADs onto MTD with a local inter-PF pattern similar to that in the native B5-B8 PFs. Such preference of inter-PF pattern may help with the landing of OADs onto MTD B-tubules during ciliogenesis and the effect could potentially be reinforced in the presence of docking complexes.

In the parallel OAD, the two ICs of core-OAD directly contact and cross over each other at multiple sites (fig. S9C), in addition to their interaction with HB3-5 of α/β-HCs. This facilitates core-OAD to locally form a tight hetero-tetrameric architecture near the WD domains (Fig. 2C). The two ICs and N-terminal dimerization domain (NDD) of α/β-HCs together enclose and position the tail region, which is primed to interact with the motor domain of another OAD. More OADs are subsequently induced to associate with each other in a TTH manner (Fig. 1B). We re-analyzed previously reported cryo-ET maps of axonemes and found all OAD arrays are assembled in the same manner in apo state across species (fig. S11) *(9, 11, 29–31)*. The TTH interfaces involve IC3, NDD and α/β-HB1-3 of OAD_0 tail region, and α/β-Linkers, β-AAA2 small subunit (β-AAA2S), β-AAA6S and β-CT-cap of OAD_{+1} head (Fig. 2, C and D, and fig. S12, A and B). Notably, the $tail_0$ calipers the β_{+1}-motor and potentially hinders its allosteric response to nucleotides unless the TTH interface is disrupted. We therefore sought to elucidate the array formation mechanism. In the absence of MTD, most free OADs are too flexible to support a stable inter-OAD interaction for array formation (fig. S1C). They transiently adopt a pre-parallel state, which is likely to facilitate a proper landing of OADs onto microtubules, but not yet ready for binding another OAD (fig. S13). It is the MTD binding that finally aligns the three motor domains, induces the LR interaction to stabilize a fully parallel architecture, and triggers multiple OADs to cooperatively associate with each other (Fig. 2E, and fig. S13, A and B). Even though the docking complex is not required for OAD array formation in vitro, it plays an important role in anchoring OADs to the right location in axoneme *(32)*.

Our cryo-EM structures reveal that the interaction network of OAD array is dramatically remodeled when β-HC moves one step ahead from MTBS-1 to MTBS-2. Alteration of MTBS is coupled with four major groups of structural changes throughout the entire OAD. First, an 18-degree rotation of between the β-stalk (fig. S14A) and β-MTBD is required for the MTBS alteration, whereas β-MTBD remains in the high microtubule-affinity in MTBS-2 (fig. S14B). Second, a gear-shift-like switch of the LR interactions among the three motor domains is involved. In MTBS-1, the β-HC constantly docks its Linker in Post-1 (Fig. 3A), while in MTBS-2, the β-Linker is precisely switched to that in Post-2 along with the β-MTBD stepping forward (Fig. 3B). On the other hand, the α-Linker fits well into a groove (Groove-1) formed by AAA3S, AAA5 extension (AAA5E) and β-CT-cap in MTBS-1, while the β-Linker matches another groove (Groove-2) between AAA2S and AAA3S of γ-Ring (fig. S14, C and D). From MTBS-1 to MTBS-2, the α-Linker docking groove on β-Ring is also switched from Groove-1 to Groove-2 along with a slight rotation in the β/γ-LR contact site (fig. S14E). Third, the local network among β-tail, γ-tail and LC3BL is remodeled. In brief, γ-Ig-PT contacts β-AAA4L PS-I with the help of γ-Kelch in MTBS-1 (Fig. 3C), while the contact site for γ-Ig-PT on the β-motor domain is switched to the H2-β3 loop of β-AAA3L in MTBS-2 (Fig. 3D). From MTBS-1 to MTBS-2, LC3BL takes over γ-Ig-PT to contact β-AAA4L at the same site. Finally, the tail is rotated downward with respect to the head from MTBS-1 to MTBS-2.

Comparing with previously reported dynein structures reveals that the ADP-bound state of cytoplasmic dynein *(33)* has a most similar Linker docking mode to that in the Post-2 conformation of OAD β-HC. The ADP-bound state is thought to represent the rebinding of dynein MTBD to microtubule after moving one step ahead *(34)*. Therefore, the β-HC in Post-2 is likely to mimic the state after one complete nucleotide cycle. After ATP treatment *(35)* on the native *T. thermophila* axonemes and reverting to ATP-free solution, we could observe both Post-1 and Post-2 states on the same cryo-ET data (fig. S1, F and G). Despite the remodeling of OAD array from MTBS-1 to MTBS-2, the pattern of TTH interac-

bioRxiv preprint doi: https://doi.org/10.1101/2020.12.08.415687; this version posted December 8, 2020. The copyright holder for this preprint (which was not certified by peer review) is the author/funder, who has granted bioRxiv a license to display the preprint in perpetuity. It is made available under aCC-BY-NC-ND 4.0 International license.

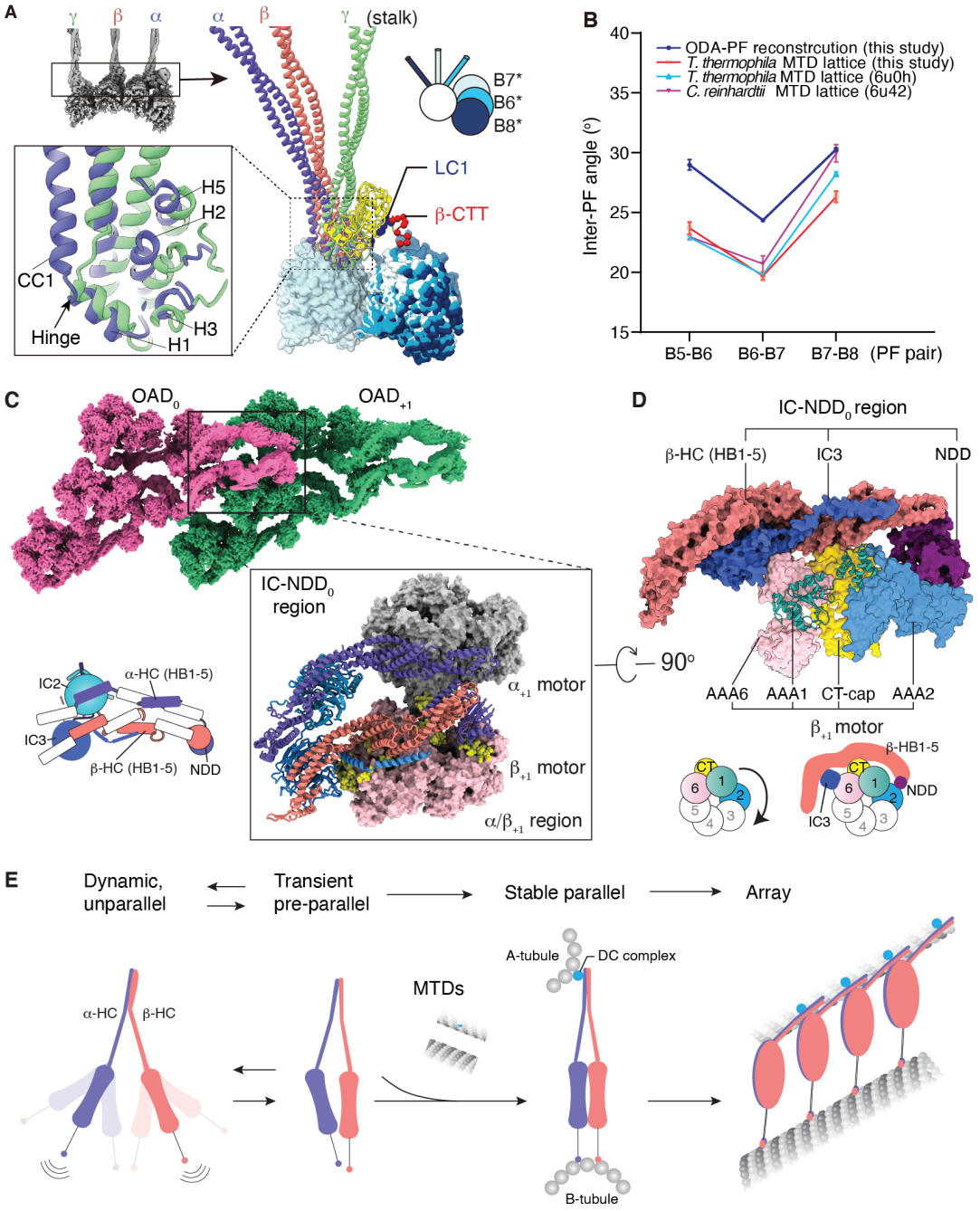

Fig. 2. A mechanism of the OAD-MTD array formation. (A) A comparison among α-, β- and γ-MTBD together with the stalks. Structures are aligned by superimposition of the three MTBD-bound protofilaments. A detailed comparison between α- and γ-MTBD is shown in the lower left inset. A model (lower right) is attached to show the relative rotations between adjacent protofilaments. Note the four protofilaments in the reconstituted OAD-PF may not necessarily be the native B5-B8 (*). **(B)** The inter-PF angle pattern in the OAD-PF reconstruction is similar to that in native B5-B8 PFs from three independent MTD studies. **(C)** The IC-HC forms a compact claw-like conformation in tail region and grasps the head region (mainly β-Ring) from an adjacent OAD unit. **(D)** Close-up view of the tail-to-head region. The schematic shows how tail_0 region calipers β_{+1}-Ring and restrains its free allosteric response. **(E)** An array formation mechanism. Most free OADs are loose, dynamic, and unparallel, while a few of them show a pre-parallel conformation. Induced by the binding of MTBDs to MTD, the motor domains are aligned to form a parallel conformation that allows the TTH interactions.

bioRxiv preprint doi: https://doi.org/10.1101/2020.12.08.415687; this version posted December 8, 2020. The copyright holder for this preprint (which was not certified by peer review) is the author/funder, who has granted bioRxiv a license to display the preprint in perpetuity. It is made available under aCC-BY-NC-ND 4.0 International license.

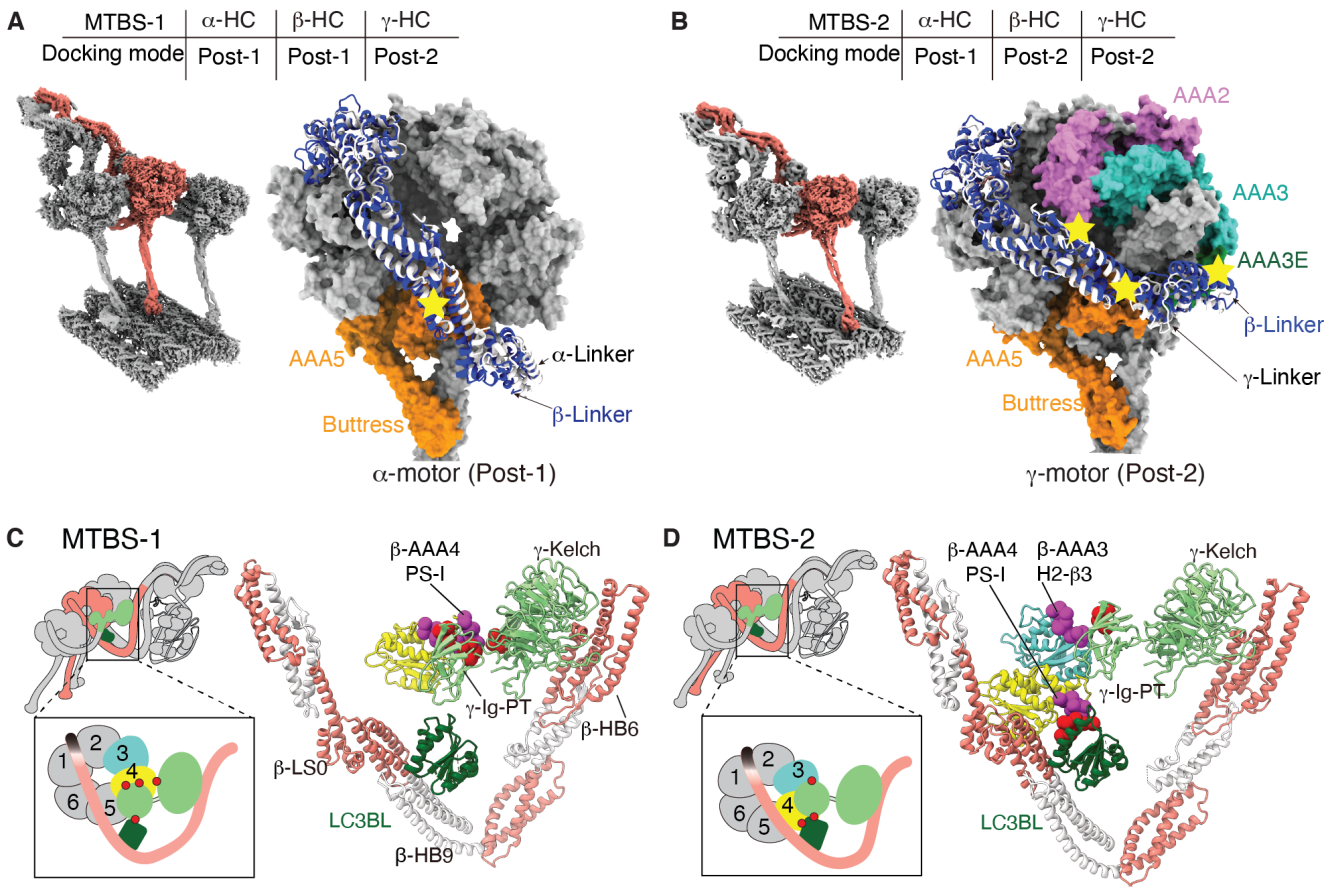

Fig. 3. Coupled conformational changes of the ODA array from MTBS-1 to MTBS-2. (A-B) The gear-shift-like LR interaction. β-Linker (blue) adopts Post-1 (classical, same as α-HC) and Post-2 (novel, same as γ-HC) docking modes in MTBS-1 (A) and MTBS-2 (B), respectively. **(C-D)** Remodeling of local interaction network around LC3BL. The AAA4 PS-I region switches its interaction with γ-Ig-PT/Kelch region in MTBS-1 **(C)** to LC3BL in MTBS-2, along with formation of a new contact between AAA3 and Ig-PT **(D)**.

tion remains nearly unchanged (fig. S14, F and G). In either MTBS, the core-OAD conformations are synchronized along the same array (fig. S14, F and G). However, the conformations in the two states are not compatible. Sterical clashes are unavoidable by substitution of OAD units between the two states (fig. S14, H and I). Therefore, the TTH interfaces need to be temporarily disrupted to complete the MTBS alteration. This is unlikely to occur within a locally synchronized OAD array except the ends or the transition points where the TTH interaction is temporarily relaxed.

What is the key factor that potentially affects the TTH interfaces? We propose two possibilities, nucleotide- and geometry-control, which can co-exist. First, we re-analyzed all previously reported cryo-ET maps of core-OADs using our atomic coordinates. An interesting finding is that the pre-powerstroke state shows a completely different interaction, in which the β-motor$_{+1}$ is thoroughly released from IC-NDD$_0$ region along with a clockwise and downward rotation, consistent across species (fig. S15A) *(12, 29, 30)*. We then tested how the reconstituted OAD-MTD arrays respond to different nucleotides. Briefly, arrays could still be observed after incubation with either AMP-PNP or ADP but completely fell off the MTDs in the presence ATP, ADP·Vi or ATPγS (fig. S15B). We speculate it is the ATP hydrolysis that releases the MTBDs from MTD and subsequently breaks the array interfaces. Using gradient concentrations of ATPγS, we were able to gradually shorten OAD arrays in vitro owing to the low hydrolysis rate. Increasing the ATPγS does not cut the array into many shorter segments randomly, but rather sequentially shortens the arrays (fig. S15C), suggesting ATP hydrolysis is more likely to take place at the ends of an ordered OAD array.

Based on our current results and previously reported OAD structures, we propose the following model for how arrayed OADs coordinate with each other to take one step (Fig. 4). In the apo state (Post-1), OADs are attached to B-tubule and form an ordered array. The TTH interactions between OAD$_0$ and OAD$_{+1}$ sterically restrain nucleotide-induced allosteric response of OAD+1 and its downstream neighbors (toward cilium tip). Curvature changes may temporally relax the array interfaces and allow free nucleotide cycle locally. After relaxation of the TTH interfaces, the OAD is free for its nucleotide cycle and energy from ATP-hydrolysis is consumed to release OAD from B-tubule, rotate the motor domain and move it one step forward. This in turn relaxes the TTH interfaces between currently active OAD and its downstream neighbors. The process is rapidly propagated to the plus end of MTD. Meanwhile, the release of phosphate groups and ADPs from upstream OADs will lead to a re-binding of OADs to B-tubule in Post-2, which subsequently imposes

bioRxiv preprint doi: https://doi.org/10.1101/2020.12.08.415687; this version posted December 8, 2020. The copyright holder for this preprint (which was not certified by peer review) is the author/funder, who has granted bioRxiv a license to display the preprint in perpetuity. It is made available under aCC-BY-NC-ND 4.0 International license.

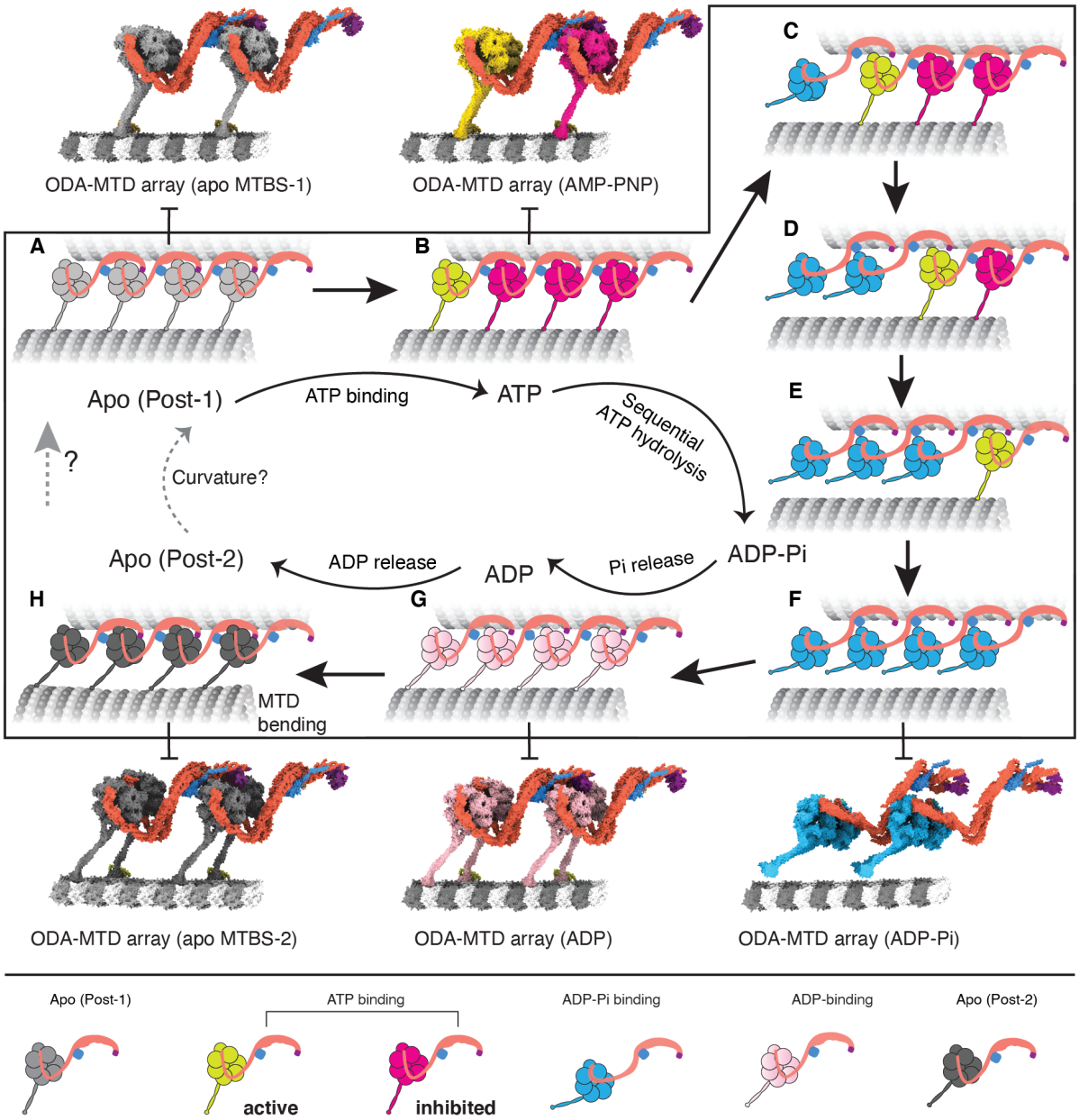

Fig. 4. A proposed model for the switch role of TTH interfaces in motor coordination. (A) An OAD-MTD array adopts Post-1 in apo state. **(B)** In the ATP-binding state, the OAD unit that has relaxed motor domains is active (yellow), while the rest are restrained by TTH interaction (magenta). **(C-F)** Once the TTH interaction is disrupted by ATP hydrolysis of the relaxed OAD, it will sequentially relax downstream OAD units along the array. **(G)** Putative model of OAD-MTD array in ADP-binding state, which is supposed to be 8 nm forward. **(H)** After ADP release, the OAD array adopts Post-2 state and bends local MTD. The models of the OAD array in ADP-Pi and ADP states were built by fitting our atomic coordinates into previously reported cryo-ET maps (EMD-5758, EMD-5619) *(12, 29)*.

tension on two adjacent MTDs. The tension is converted to local bending of MTD (fig. S16), which is propagated towards the plus end along with the nucleotide cycle propagation.

Our current cryo-EM structures of OAD arrays and the proposed model potentially explain how a rhythmic ciliary beat is generated through phased propagation of OAD nucleotide states and microtubule-binding states. The results also raise many more interesting questions, such as how the three motor domains coordinate their nucleotide cycles and microtubule-binding states, how the MTD-bending curvatures quantitatively affect the binding affinity of OADs to MTD, and how γ-HC, LCs, IDAs, DRCs as well as extracellular signals collectively regulate the OAD array activities.

Materials and methods

Purification of OAD and MTD

Mucocyst-deficient strain *T. thermophila* SB715 *(26)* was purchased from Tetrahymena Stock Center (Cornell University, https://tetrahymena.vet.cornell.edu/). The axoneme was purified by using a modified dibucaine method *(36)* from 4 liters of culture for each sample preparation. In brief, the pellet from every one-liter fresh cell culture was de-ciliated with 3 mM dibucaine (Sigma-Aldrich) in 150 mL fresh SSP medium, and centrifuged at 2, 000 xg for 10 min to remove

bioRxiv preprint doi: https://doi.org/10.1101/2020.12.08.415687; this version posted December 8, 2020. The copyright holder for this preprint (which was not certified by peer review) is the author/funder, who has granted bioRxiv a license to display the preprint in perpetuity. It is made available under aCC-BY-NC-ND 4.0 International license.

the cell body. The cilia were spun down from the supernatant at 12, 000 xg for 10 min, resuspended by axoneme buffer (20 mM HEPES pH 7.4, 100 mM NaCl, 2 mM MgCl2, 1 mM DTT), and further demembranated with 1.0% TritonX-100 in axoneme buffer. The axoneme was then pre-treated with buffer containing high potassium acetate (HPA buffer 50 mM HEPES pH 7.4, 600 mM CH3COOK, 5 mM MgSO4, 0.5 mM EGTA, 1 mM PMSF, 1 mM DTT) for 30 min. Subsequently, the purified axonemes were treated in different conditions for different assays. For OAD purification, the axoneme was treated with high-salt buffer (HSC buffer 50 mM HEPES pH 7.4, 600 mM NaCl, 5 mM MgSO4, 0.5 mM EGTA, 1 mM PMSF, 1 mM DTT), and incubated on ice for 30 min. MTD and the majority of axonemal dyneins were separated by centrifugation at 21,000 xg for 10 min for further purification. To obtain high-quality OAD complex from the supernatant, we used an OAD extraction protocol *(37)* and optimized the parameters in our own experiments. The supernatant was laid over 5-25% (w/v) linear sucrose gradients in OAD buffer (50 mM HEPES pH 7.4, 100 mM NaCl, 1 mM DTT) and centrifuged at 153, 000 xg for 16 h at 4°C. The gradient was fractionated into 0.2 mL aliquots. Fractions containing IDAs and OAD were determined by SDS-PAGE (4-20% Mini-PROTEAN TGX precast protein gels run in SDS buffer (Bio-Rad)), stained by SYPRO Ruby or Page-Blue staining solution. The pooled fractions containing the OAD were dialyzed (REPLIGEN dialysis membranes) against the OAD buffer for 6h at 4 °C to remove the sucrose and then loaded on an EnrichQ 5/50 column (Bio-Rad) equilibrated with the ion-exchange buffer A (50 mM HEPES pH 7.4, 50 mM KCl, 1 mM DTT). The OAD was eluted with a linear salt gradient: 0-50% buffer B (with 1 M KCl) in 8 mL. The fractions containing OAD were determined by SDS-PAGE (Bio-Rad), pooled together, and adjusted to a final concentration of 0.3 mg/mL for reconstitution assay. The MTD pellet was resuspended in high salt buffer and dialyzed against the low salt buffer (50 mM HEPES pH 7.4, 0.5 mM EDTA, 1 mM DTT) overnight at 4°C *(35)*. The MTD was then pelleted and resuspended with the fresh low salt buffer. The final concentration was adjusted to 0.6 mg/mL for the subsequent reconstitution assay. Grafix method *(38)* was used to improve the quality of free OAD samples for EM analysis. Briefly, the OAD fractions from the linear sucrose gradient were collected, dialyzed against the OAD buffer, concentrated to 1 mL and applied to Grafix [0-0.0125% (v/v) linear glutaraldehyde (Sigma-Aldrich) gradients along with a 5-25% (w/v) linear sucrose gradient in the OAD buffer]. The gradient was fractionated into 0.2 mL aliquots. The crosslinking was quenched by adding 10 µL Tris-HCl (1 M, pH 8.0) to each aliquot. The fractions containing the cross-linked OAD were determined by SDS-PAGE (Bio-Rad) and evaluated by ns-EM. The fractions containing properly cross-linked OAD were dialyzed against the OAD buffer for 6 h, concentrated to 50 µL and loaded to the TSKgel G4000SWXL column (TOSOH Bioscience) equilibrated with the gel filtration buffer (20 mM HEPES pH 7.4, 100 mM KCl, 1 mM DTT, 2 mM MgSO4). The peak fractions were pooled for subsequent negative-stain analysis. Protein concentrations were measured by using BioSpectrometer (Eppendorf).

Mass spectrometry

Mass spectrometry (MS) on the isolated OAD sample was performed at Keck Biotechnology Resource Laboratory, Yale University. The OAD subunits identified from the MS data are summarized in table S1.

Microtubule gliding assay and analysis

Dynein gliding assay was adapted from a previously published protocol *(39)*. In brief, HMDE buffer (30 mM HEPES-KOH, 5 mM MgSO4, 1 mM EGTP, 1 mM DTT, pH 7.4) was first introduced into the flow channel, followed by a 5-min incubation of 10 µL, 0.1 mg/mL purified outer arm dynein at room temperature to allow adsorption of dynein to the coverglass surface. Unbound dynein was then washed with HMDE buffer, followed by a 5-min incubation of 0.4 mg/mL casein. The channel was again washed by HMDE buffer. GMPCPP-stabilized microtubules were prepared as previously described *(40)* using bovine brain tubulin purified in-house *(41)*. 10 µL of microtubule solution (0.15 µM tubulin dimer in HMDE + 1 mM ADP) was perfused in to bind to the motors with a subsequent wash by HMDE+1 mM ADP. 10 µL motility solution (HMDE + 1 mM ATP + 1 mM ADP) was then flowed in to initiate the microtubule gliding, imaged by interference reflection microscopy (IRM) as previously described *(42)*(41) with a frame rate of 13.5 Hz. Lengths and positions along the gliding paths of individual microtubules were tracked with tracking software FIESTA *(43)* after background subtraction. Tracking results were manually inspected to exclude immobile filaments, surface dirt particles, tracks less than 1 second, and tracking errors due to filament collisions. Position of individual microtubule filament was averaged over three frames (0.22 s interval) to reduce the experimental noise. Time-weighted average velocity and displacement-weighted average velocity were calculated as previously described *(44)* with the bin width of 0.4 µm/s. The standard error of the mean (SEM) of the displacement-weighted average velocity is equal to the standard deviation (SD) divided by $\sqrt{N}$, where N is the number of microtubules in each condition (N=51, 75, 65, 78 MTs for 100, 50, 20, 10 µg/mL of ODA with wildtype GMPCPP-microtubule, and N=51 for 100 µg/mL ODA with subtilisin-treated GMPCPP microtubule). P-value was calculated using Welch's t-test.

OAD-MTD array reconstitution and nucleotide treatment

The reconstitution condition was optimized from our cryo-EM analysis based on a previously published protocol *(6)*.To assemble the OAD-MTD complex, the freshly purified native OAD (not cross-linked) and MTD samples were mixed at a series of molar ratios (tubulin dimer/ OAD, 10-100) in the reconstitution buffer (20 mM Hepes pH 7.4, 100 mM KCl, 5 mM MgSO4, 1 mM DTT) and incubated on ice for 45 min. The reconstituted samples were analyzed by SDS-PAGE

bioRxiv preprint doi: https://doi.org/10.1101/2020.12.08.415687; this version posted December 8, 2020. The copyright holder for this preprint (which was not certified by peer review) is the author/funder, who has granted bioRxiv a license to display the preprint in perpetuity. It is made available under aCC-BY-NC-ND 4.0 International license.

and negative-stain electron microscopy to screen out the optimal molar ratio. The concentration of the OAD-MTD complex was optimized by centrifugation and resuspension for subsequent experiments and checked by cryo-EM. All protein samples were verified by 4-20% Mini-PROTEAN TGX precast protein gel stained with Page-Blue solution. After array formation (45 nM OAD), different nucleotides at a final concentration of 1 mM or ATPγS at gradient concentrations were added to the reconstitution tubes. 4 µL solution in each reaction condition was immediately transferred to a glow-discharged continuous carbon grid (Electron Microscopy Sciences) for 15 seconds before blotting and staining. The grid was stained with 2% uranyl acetate and air-dried before loading to a Talos L120C microscope (Thermo Fisher Scientific). The length of the array was directly measured in the ImageJ and converted to the equivalent number of OADs for subsequent quantitative analysis.

Cryo-EM sample preparation and data collection

4 µL OAD or OAD-MTD samples were applied to each Quantifoil R2/2 or C-flat R1.2/1.3 gold grid (for free OAD, the grids were coated a carbon layer), incubated in a Vitrobot Mark IV (Thermo Fisher Scientific) for 4 seconds, blotted for 2 seconds at 4 °C and 100% humidity, and then plunged into liquid ethane near melting point. Three cryo-EM datasets of ODA-MTD arrays in the apo state were collected on a 300 keV Titan Krios microscope (Thermo Fisher Scientific) equipped with a Bioquantum Energy Filter and a K2 Summit direct electron detector (Gatan) at Yale CCMI Electron Microscopy Facility. Data collection was automated by Serial EM software *(45)* and all micrographs were recorded in a super-resolution mode. The first two data sets were employed with the following parameters: 0.822 Å/pixel, 50 µm C2 aperture, 32 frames, 53.3 e-/Å2, 8 s exposure, -0.8 to -2.0 µm defocus range. Based on the results of these two data sets, the third data acquisition was optimized with a reasonable parameter set as follows: 1.333 Å/pixel, 50 µm C2 aperture, 40 frames, 53.3 e-/Å2, 12 s exposure, -1.2 to -3.0 µm defocus range. Three non-overlapping micrographs were recorded per hole in all the three data sets. The motion correction, particle picking, and CTF estimation were streamlined to evaluate the micrograph quality in real time during the data collection using a modified pre-processing script (https://www2.mrc-lmb.cam.ac.uk/research/locally-developed-software/zhang-software).

Cryo-ET data collection and reconstruction

Purified axonemes were treated with ATP at a final concentration of 1 mM for 5 minutes and reverted to nucleotide-free solution before freezing for cryo-ET. In total, 50 tomographic datasets were collected on the 300kV Titan Krios equipped with a K2 detector. The software SerialEM *(45)* was used for automatic data collection under the bidirectional scheme at a 3° interval and tilt angles ranging from -51° and +51°. Each of the final tilt series contains 35 movies with a pixel size of 2.8 Å at an average defocus of 5 µm and a total dose of 70 e/Å2. Individual movies were aligned by MotionCor2 *(46)*. Motion-corrected images of each tilt series were aligned by using the patch-alignment approach in the IMOD software *(47, 48)*. Sub-volume average was performed using PEET *(49)*.

Pre-processing of cryo-EM data

Beam-induced drift was corrected using MotionCor2 *(46)* for all images. CTF parameters for each motion-corrected micrograph were estimated using Gctf *(50)*. All particles were automatically picked using Gautomatch, extracted in RELION v3.0 *(51)* and imported to cryoSPARC v2.12 *(52)* for all subsequent processing, if not explicitly stated otherwise.

Structure determination of MTD

To obtain and analyze the structure of MTD, we first manually picked a small dataset (100 micrographs) at 4-nm intervals from Dataset 1 (table S1). These particles were analyzed in Cryosparc v2.12 to generate 20 good MTD 2D averages and used by Gautomatch for template-based particle picking. This generated 444, 603 raw particles from Datasets 1 and 2, and 680, 495 raw particles from Dataset 3 using a 4-nm distance cutoff (if the distance between two particles is less than 4 nm, the one with lower cross-correlation coefficient is removed). All the particles were extracted with a box size of 512 × 512. The micrographs from Dataset 1 and Dataset 2 were both scaled to a pixel size of 1.333 Å to match the Dataset 3 during the particle extraction. After 3-5 cycles of 2D classification to remove those particles that generated bad 2D averages, the high-quality images we selected and filtered by a 6-nm distance cutoff. This reduced the sampling of MTD to 8 nm and yielded 358, 116 good particles for subsequent 3D analysis. A previous MTD map from *T. thermophila* (EMDB: 8532) *(35)* was low-passed to 100 Å as an initial model. The 8-nm repeats were successfully separated into two classes of 16-nm repeats with comparable particles numbers after 3D classification in cryoSPARC v2.12 (51). The two 16-nm repeating maps were essentially the same except that they were shifted 8 nm with respect to each other. 196,740 good particles with 16-nm periodicity were selected for subsequent analysis. By restricting the refinement to each local region with 3 × 4 tubulins, we were able to improve the local tubulins at an average resolution of 3.1Å. A *de novo* model of the tubulin dimer was built on the best region and then expanded to all regions for manual refinement in Coot *(53)* and automatic refinement by Refmac5 *(54)*. The 16-nm MTD repeat was used to estimate inter-PF distribution of tubulin lattice. Other structural information from MTD reconstruction using different parameters was not used in this work.

Structure determination of OAD-PF

To eliminate the interference of microtubule in OAD structure determination, we linearly weakened the microtubule signals to improve the alignment of OAD. In brief, the coordinates of all good particles we selected during the MTD

bioRxiv preprint doi: https://doi.org/10.1101/2020.12.08.415687; this version posted December 8, 2020. The copyright holder for this preprint (which was not certified by peer review) is the author/funder, who has granted bioRxiv a license to display the preprint in perpetuity. It is made available under aCC-BY-NC-ND 4.0 International license.

reconstruction were split and backtracked to their original micrographs. We manually checked all micrographs one by one to make sure they are centered and evenly spaced in each MTD. If not, we then manually adjusted the uncentered, added the missing particles, or deleted the undesirable ones. The MTD signal was weakened by removing the weighted average within a rectangle mask slightly wider than the MTD. The OAD particles from the MTD-weakened micrographs were picked by Gautomatch using 20 best templates generated from a negative-stain dataset of free OAD. After 2D classification, we selected the fifty best 2D averages for another cycle of automatic particle picking. Due to the severe orientation preference, we used a very low cross-correlation (CC) cutoff (0.08) and also a very small distance cutoff (150 Å) for automatic picking by Gautomatch. The purpose was to include as many views as possible at the beginning even if there were some false pickings. This generated 824, 659 particles from Dataset 1 and 2, and 2, 022, 385 particles from Dataset 3. Cycles of 2D and 3D classification (for screening purpose) were performed on the 8 times shrunk images to remove MTDs and low-quality particles. In total, 346, 320 good particles were selected for subsequent 2D and 3D analysis. All particles from the above processing were re-extracted with a box size of 510 × 510 at 1.333 Å pixel size (Dataset 1 and 2 were re-scaled to this pixel size) and merged for subsequent processing. To further remove particles that were less consistent with the major classes, we performed iterative 2D and 3D classification. Briefly, all the particles were separated into four subsets to accelerate the processing. Each cycle of 2D cycle was followed by two cycles of 3D classification. 58, 096 particles were further excluded via this 2D and 3D classification. All the subsets were merged again that yielded 288, 224 good particles for a final cycle of 3D classification. This generated nine good classes and one bad class. Six of the nine classes were categorized to microtubule-binding state 1 (MTBS-1), while the rest three were in MTBS-2. At this stage, we had 191, 776 particles in MTBS-1 and 76, 936 for subsequent local refinement. A multi-level masking scheme was applied to the local refinement. Briefly, we gradually decreased the size of the mask applied to a certain region to ensure a stable local refinement. We divided each of the OAD-PF class into five major parts: (a) MTBD-tubulin region, (b) α-motor domain, (c) β-motor domain, (d) γ-motor domain, (e) tail region. The α-motor domain in MTBS-1 was straightforward improved from 10.1 Å to 4.5 Å after one cycle of local refinement. At such resolution, we were able to build backbones, but ab-initio assignment of the side chains was very challenging. The map was further improved by optimizing the following aspects: (i) more cycle of local classification, (ii) refinement of the particle centers, (iii) manual optimization of the local mask, (iv) 2D classification based on 3D alignment parameters, (v) local CTF refinement, (vi) non-uniform refinement *(55)*. By combining these approaches in an iterative way, the map of α-motor domain was finally improved to an average resolution of 3.19 Å resolution for final model building. We applied the same strategy to improve the β-motor domain which finally generated a map at 3.3 Å resolution overall. Focusing on the AAA2-4 subdomains allowed us to slightly improve this region which helped with the model building a bit. The γ-motor domain, MTBD region and tail region are much more complicated than the other two. We were able to overcome the issue by. To ensure that the maps from two adjacent regions can be smoothly combined, we applied a third mask that fully covered the boundary between each pair of adjacent masks. Finally, we integrated all 31 locally refined parts into an entire unit of OAD-PF array in Chimera *(56)*. The structures of free OAD and OAD-PF in the AMP-PNP bound state were determined using the same approach.

Identification of the light chains

We built the atomic model of all the ten IC-binding light chains de novo in combination with our mass spectrometry data. First, each of the ten LCs was manually built as a poly-Ala model. All side chains were tentatively assigned to several groups: (1) large (Trp, Try, Arg, Phe, His), (2) middle (Leu, Gln, Asn, Ile, Met, Lys), (3) small (Pro, Val, Ser, Thr, Cys, Glu, Asp, Ala), and (5) Gly. Here we categorized Glu and Asp into the group 'small' because the side chain densities of negatively charged residues are typically weak in cryo-EM reconstruction. We then performed two parallel approaches to identify all the light chains: (a) pattern recognition and (b) penalty function. The approach (a) is based on regular expression match using the 'gawk' command on a CentOS 7.5 Linux system. In the second approach, we tried to fit all predicted homologs into a certain position, e.g. the LC8-2b position and assigned the residues. All the residues that did not match the side-chain density were manually counted. The counts were regarded as penalty scores for all LC homologs. We then compared the final scores and selected the best one for subsequent model building and refinement. A protein was regarded as 'identified' only if it meets the following requirements: (i) it exists as a significant hit from the mass spectrometry data; (ii) its side chains simultaneously match the cryo-EM density map; (iii) no other homologs have better results of (i) or (ii). We identified IC2, IC3, γ-Kelch, all the ten IC-binding light chains. The LC7-a/b is not the standard LC7A/B heterodimer, but a heterodimer comprising LC7B (LC7-b) and an unnamed LC7A homolog (TTHERM_00348650). The full-length protein is 159 residues long (XP_976918.2) while the truncated one is 103 residues long (XP_976918.1). We unambiguously assigned the residues from S58 to G152. The extra density that links γ-HB6 to LC7-b was tentatively assigned as the N-terminus of LC7-b. Despite the similar core structures, each of the six LC8-like proteins (LC8s) are clearly different from any other five by its characteristic side chain densities and loops, which allowed us to distinguish them unambiguously. The positions of 1a, 1b, and 2a are taken by LC10, DLC82 and LC8E, respectively. The rest three (2b, 3a, 3b) were simply predicted to be LC8 homologs without standard names in TGD (TTHERM_00023950 for LC8-2b, TTHERM_01079060 for LC8-3a and TTHERM_000442909

bioRxiv preprint doi: https://doi.org/10.1101/2020.12.08.415687; this version posted December 8, 2020. The copyright holder for this preprint (which was not certified by peer review) is the author/funder, who has granted bioRxiv a license to display the preprint in perpetuity. It is made available under aCC-BY-NC-ND 4.0 International license.

for LC8-3b). Neither TCT1A nor TCT1B matched the key features of our cryo-EM maps. The Tctex-a position was identified as a hypothetical homolog (TTHERM_00392979) while the best hit for Tctex-b is LC2A *(57)*.

Model Building and Refinement

We used different model building approaches for different regions. Most of the regions were refined at better than 3.5 Å resolution, which allowed us to build them in Coot *(53, 58)* with side chains assigned and refined ab initio. For the regions that were slightly worse, we were able to build backbone models with the residues assigned based on the relative positions among the large resides (such as Try and Arg) of each domain. For the regions that show clear backbone density with low-quality sidechain density, we coarsely assigned the residues using previously published homologous structures as references or predicted model from Phyre2 web server *(59)*. For those regions that were solved at a resolution with helices clearly separated, we fitted the predicted model into the density as rigid bodies in Chimera *(56)*. If the predicted model contained more than one subdomain, we then refined the fitting of each subdomain as a rigid body in Coot *(58)*. All models at better than 4 Å resolution were automatically refined by Refmac5 *(59)*, followed by manual check in Coot *(58)*. The process was repeated until all parameters were reasonably refined.

Inter-PF rotation angle measurement

The inter-PF angle is defined as the lateral rotation angles between a pair of adjacent microtubule protofilaments, as described in a previous publication *(25)*. To calculate the inter-PF angle of MTD, we fitted individual tubulin dimer model built from the 16-nm MTD reconstruction into the 48-nm MTD map as rigid bodies. We calculated the inter-PF angle between each pair of tubulin dimers throughout each protofilament. The averaged value and standard deviation were estimated from the six measurements along each protofilament. All the inter-PF angles were calculated in PyMOL (https://pymol.org/2/).

MTD curvature analysis

After manual checking all the micrographs, we selected 15, 541 MTDs in total. Using the manually verified coordinates, the curve of each MTD was approximated with a polynomial regression of degree 3. All curves were resampled with a sampling rate of 4 nm. The axial direction of MTD at each point was estimated as the tangent line. The curvature of the fitted curve at each resampled point was calculated to approximate the local MTD bending. The maximum orientation difference among all the tangent lines of each MTD was regarded as the bending angle.

Visualization and representation

The figures and movies were created by Chimera *(56)*, ChimeraX *(60)* and PyMOL (https://pymol.org/2/). Other tools used in this research include FIJI *(61)*, EMAN2 *(62)* and ESPript *(63)*. This manuscript for BioRxiv was formatted using a modified LaTeX template from the Henriques Lab (https://www.overleaf.com/latex/templates/henriqueslab-biorxiv- template/nyprsybwffws.Wp8hF1Cnx-E)

ACKNOWLEDGEMENTS

We thank S. Wu, K. Zhou, M. Llaguno and K. Li for technical support on microscopy, J. Kanyo for mass spectrometry support, Y. Xiong, F. Sigworth, J. Liu, and S. Baserga for their valuable research advice, S.M. King, A. Yildiz, A.P. Carter and Y. Xiong for valuable feedback on the manuscript, and P. Sung, W. Konigsberg, A. Garen, Y. Xiong as well as many others for their generous support during K.Z.'s lab setup. **Funding:** This work was supported by start-up funds from Yale University and Rudolf J. Anderson Fellowship awards to L.H. and Y.W. **Author contributions:** Q.R. prepared all samples and performed biochemical characterization; Q.R., K.Z., P.C., Y.W., L.H., R.Y., and Y.Y. determined the apo ODA-PF structures; P.C., K.Z. and Q.R. determined all other structures in this work; Q.R. and Y-W.K. performed motility assays; all involved in analyzing the results; K.Z. and Q.R. prepared the manuscript with the help from all other co-authors. **Competing interests:** None. **Data availability:** Cryo-EM maps and atomic coordinates have been deposited in the Electron Microscopy Data Bank under accession codes EMD-22677, EMD-22679, EMD-22840, EMD-XXXX and in the Protein Data Bank in under accession 7K58, 7K5B, 7KEK, XXXX.

References:

1. S. M. King. Axonemal dynein arms. *Cold Spring Harb Perspect Biol*, 8 (11), 2016. ISSN 1943-0264 (Electronic) 1943-0264 (Linking). doi: 10.1101/cshperspect.a028100.
2. R. Viswanadha, W. S. Sale, and M. E. Porter. Ciliary motility: Regulation of axonemal dynein motors. *Cold Spring Harb Perspect Biol*, 9(8), 2017. ISSN 1943-0264 (Electronic) 1943-0264 (Linking). doi: 10.1101/cshperspect.a018325.
3. L. Bartoloni, J. L. Blouin, Y. Pan, C. Gehrig, A. K. Maiti, N. Scamuffa, C. Rossier, M. Jorissen, M. Armengot, M. Meeks, H. M. Mitchison, E. M. Chung, C. D. Delozier-Blanchet, W. J. Craigen, and S. E. Antonarakis. Mutations in the dnah11 (axonemal heavy chain dynein type 11) gene cause one form of situs inversus totalis and most likely primary ciliary dyskinesia. *Proc Natl Acad Sci U S A*, 99(16):10282–6, 2002. ISSN 0027-8424 (Print) 0027-8424 (Linking). doi: 10.1073/pnas.152337699.
4. N. Hornef, H. Olbrich, J. Horvath, M. A. Zariwala, M. Fliegauf, N. T. Loges, J. Wildhaber, P. G. Noone, M. Kennedy, S. E. Antonarakis, J. L. Blouin, L. Bartoloni, T. Nusslein, P. Ahrens, M. Griese, H. Kuhl, R. Sudbrak, M. R. Knowles, R. Reinhardt, and H. Omran. Dnah5 mutations are a common cause of primary ciliary dyskinesia with outer dynein arm defects. *Am J Respir Crit Care Med*, 174(2):120–6, 2006. ISSN 1073-449X (Print) 1073-449X (Linking). doi: 10.1164/rccm.200601-084OC.
5. E. Escudier, P. Duquesnoy, J. F. Papon, and S. Amselem. Ciliary defects and genetics of primary ciliary dyskinesia. *Paediatr Respir Rev*, 10(2):51–4, 2009. ISSN 1526-0550 (Electronic) 1526-0542 (Linking). doi: 10.1016/j.prrv.2009.02.001.
6. T. Oda, T. Abe, H. Yanagisawa, and M. Kikkawa. Docking-complex-independent alignment of chlamydomonas outer dynein arms with 24-nm periodicity in vitro. *J Cell Sci*, 129(8):1547–51, 2016. ISSN 1477-9137 (Electronic) 0021-9533 (Linking). doi: 10.1242/jcs.184598.
7. K. Zhang, H. E. Foster, A. Rondelet, S. E. Lacey, N. Bahi-Buisson, A. W. Bird, and A. P. Carter. Cryo-em reveals how human cytoplasmic dynein is auto-inhibited and activated. *Cell*, 169(7):1303–1314 e18, 2017. ISSN 1097-4172 (Electronic) 0092-8674 (Linking). doi: 10.1016/j.cell.2017.05.025.
8. S. Aoyama and R. Kamiya. Strikingly fast microtubule sliding in bundles formed by chlamydomonas axonemal dynein. *Cytoskeleton (Hoboken)*, 67 (6):365–72, 2010. ISSN 1949-3592 (Electronic) 1949-3592 (Linking). doi: 10.1002/cm.20450.
9. D. Stoddard, Y. Zhao, B. A. Bayless, L. Gui, P. Louka, D. Dave, S. Suryawanshi, R. F. Tomasi, P. Dupuis-Williams, C. N. Baroud, J. Gaertig, M. Winey, and D. Nicastro. Tetrahymena rib72a and rib72b are microtubule inner proteins in the ciliary doublet microtubules. *Mol Biol Cell*, 29(21):2566–2577, 2018. ISSN 1939-4586 (Electronic) 1059-1524 (Linking). doi: 10.1091/mbc.E18-06-0405.
10. M. Ma, M. Stoyanova, G. Rademacher, S. K. Dutcher, A. Brown, and R. Zhang. Structure of the decorated ciliary doublet microtubule. *Cell*, 179(4):909–922 e12, 2019. ISSN 1097-4172 (Electronic) 0092-8674 (Linking). doi: 10.1016/j.cell.2019.09.030.
11. T. Kubo, Y. Hou, D. A. Cochran, G. B. Witman, and T. Oda. A microtubule-dynein tethering complex regulates the axonemal inner dynein f (i1). *Mol Biol Cell*, 29(9):1060–1074, 2018. ISSN 1939-4586 (Electronic) 1059-1524 (Linking). doi: 10.1091/mbc.E17-11-0689.
12. T. Movassagh, K. H. Bui, H. Sakakibara, K. Oiwa, and T. Ishikawa. Nucleotide-induced global conformational changes of flagellar dynein arms revealed by in situ analysis. *Nat Struct Mol Biol*, 17(6):761–7, 2010. ISSN 1545-9985 (Electronic) 1545-9985 (Linking). doi: 10.1038/nsmb.1832.

bioRxiv preprint doi: https://doi.org/10.1101/2020.12.08.415687; this version posted December 8, 2020. The copyright holder for this preprint (which was not certified by peer review) is the author/funder, who has granted bioRxiv a license to display the preprint in perpetuity. It is made available under aCC-BY-NC-ND 4.0 International license.

13. T. Oda, T. Yagi, H. Yanagisawa, and M. Kikkawa. Identification of the outer-inner dynein linker as a hub controller for axonemal dynein activities. *Curr Biol*, 23(8):656–64, 2013. ISSN 1879-0445 (Electronic) 0960-9822 (Linking). doi: 10.1016/j.cub.2013.03.028.
14. T. Oda, T. Abe, H. Yanagisawa, and M. Kikkawa. Structure and function of outer dynein arm intermediate and light chain complex. *Mol Biol Cell*, 27 (7):1051–9, 2016. ISSN 1939-4586 (Electronic) 1059-1524 (Linking). doi: 10.1091/mbc.E15-10-0723.
15. H. Sakakibara, D. R. Mitchell, and R. Kamiya. A chlamydomonas outer arm dynein mutant missing the alpha heavy chain. *J Cell Biol*, 113(3):615–22, 1991. ISSN 0021-9525 (Print) 0021-9525 (Linking). doi: 10.1083/jcb.113.3.615.
16. M. Sakato and S. M. King. Calcium regulates atp-sensitive microtubule binding by chlamydomonas outer arm dynein. *J Biol Chem*, 278(44):43571–9, 2003. ISSN 0021-9258 (Print) 0021-9258 (Linking). doi: 10.1074/jbc.M305894200.
17. A. Harrison, M. Sakato, H. W. Tedford, S. E. Benashski, R. S. Patel-King, and S. M. King. Redox-based control of the gamma heavy chain atpase from chlamydomonas outer arm dynein. *Cell Motil Cytoskeleton*, 52(3):131–43, 2002. ISSN 0886-1544 (Print) 0886-1544 (Linking). doi: 10.1002/cm.10044.
18. A. Toda, Y. Nishikawa, H. Tanaka, T. Yagi, and G. Kurisu. The complex of outer-arm dynein light chain-1 and the microtubule-binding domain of the gamma heavy chain shows how axonemal dynein tunes ciliary beating. *J Biol Chem*, 295(12):3982–3989, 2020. ISSN 1083-351X (Electronic) 0021-9258 (Linking). doi: 10.1074/jbc.RA119.011541.
19. M. Ichikawa, K. Saito, H. A. Yanagisawa, T. Yagi, R. Kamiya, S. Yamaguchi, J. Yajima, Y. Kushida, K. Nakano, O. Numata, and Y. Y. Toyoshima. Axonemal dynein light chain-1 locates at the microtubule-binding domain of the gamma heavy chain. *Mol Biol Cell*, 26(23):4236–47, 2015. ISSN 1939-4586 (Electronic) 1059-1524 (Linking). doi: 10.1091/mbc.E15-05-0289.
20. D. R. Mitchell and K. S. Brown. Sequence analysis of the chlamydomonas alpha and beta dynein heavy chain genes. *J Cell Sci*, 107 (Pt 3):635–44, 1994. ISSN 0021-9533 (Print) 0021-9533 (Linking).
21. H. Schmidt, E. S. Gleave, and A. P. Carter. Insights into dynein motor domain function from a 3.3-a crystal structure. *Nat Struct Mol Biol*, 19(5):492–7, S1, 2012. ISSN 1545-9985 (Electronic) 1545-9985 (Linking). doi: 10.1038/nsmb.2272.
22. A. P. Carter, C. Cho, L. Jin, and R. D. Vale. Crystal structure of the dynein motor domain. *Science*, 331(6021):1159–65, 2011. ISSN 1095-9203 (Electronic) 0036-8075 (Linking). doi: 10.1126/science.1202393.
23. G. Bhabha, H. C. Cheng, N. Zhang, A. Moeller, M. Liao, J. A. Speir, Y. Cheng, and R. D. Vale. Allosteric communication in the dynein motor domain. *Cell*, 159(4):857–68, 2014. ISSN 1097-4172 (Electronic) 0092-8674 (Linking). doi: 10.1016/j.cell.2014.10.018.
24. M. A. Schlager, H. T. Hoang, L. Urnavicius, S. L. Bullock, and A. P. Carter. In vitro reconstitution of a highly processive recombinant human dynein complex. *EMBO J*, 33(17):1855–68, 2014. ISSN 1460-2075 (Electronic) 0261-4189 (Linking). doi: 10.15252/embj.201488792.
25. M. Ichikawa, A. A. Z. Khalifa, S. Kubo, D. Dai, K. Basu, M. A. F. Maghrebi, J. Vargas, and K. H. Bui. Tubulin lattice in cilia is in a stressed form regulated by microtubule inner proteins. *Proceedings of the National Academy of Sciences of the United States of America*, 116(40):19930–19938, 2019. ISSN 0027-8424. doi: 10.1073/pnas.1911119116.
26. J. C. Gutierrez and E. Orias. Genetic characterization of tetrahymena thermophila mutants unable to secrete capsules. *Dev Genet*, 13(2):160–6, 1992. ISSN 0192-253X (Print) 0192-253X (Linking). doi: 10.1002/dvg.1020130210.
27. S. M. King and R. S. Patel-King. Functional architecture of the outer arm dynein conformational switch. *J Biol Chem*, 287(5):3108–22, 2012. ISSN 1083-351X (Electronic) 0021-9258 (Linking). doi: 10.1074/jbc.M111.286211.
28. A. P. Carter, J. E. Garbarino, E. M. Wilson-Kubalek, W. E. Shipley, C. Cho, R. A. Milligan, R. D. Vale, and I. R. Gibbons. Structure and functional role of dynein's microtubule-binding domain. *Science*, 322(5908):1691–5, 2008. ISSN 1095-9203 (Electronic) 0036-8075 (Linking). doi: 10.1126/science.1164424.
29. J. Lin, K. Okada, M. Raytchev, M. C. Smith, and D. Nicastro. Structural mechanism of the dynein power stroke. *Nat Cell Biol*, 16(5):479–85, 2014. ISSN 1476-4679 (Electronic) 1465-7392 (Linking). doi: 10.1038/ncb2939.
30. H. Ueno, K. H. Bui, T. Ishikawa, Y. Imai, T. Yamaguchi, and T. Ishikawa. Structure of dimeric axonemal dynein in cilia suggests an alternative mechanism of force generation. *Cytoskeleton (Hoboken)*, 71(7):412–22, 2014. ISSN 1949-3592 (Electronic) 1949-3592 (Linking). doi: 10.1002/cm.21180.
31. J. Lin, W. Yin, M. C. Smith, K. Song, M. W. Leigh, M. A. Zariwala, M. R. Knowles, L. E. Ostrowski, and D. Nicastro. Cryo-electron tomography reveals ciliary defects underlying human rsph1 primary ciliary dyskinesia. *Nat Commun*, 5:5727, 2014. ISSN 2041-1723 (Electronic) 2041-1723 (Linking). doi: 10.1038/ncomms6727.
32. A. Onoufriadis, T. Paff, D. Antony, A. Shoemark, D. Micha, B. Kuyt, M. Schmidts, S. Petridi, J. E. Dankert-Roelse, E. G. Haarman, J. M. Daniels, R. D. Emes, R. Wilson, C. Hogg, P. J. Scambler, E. M. Chung, Uk10K, G. Pals, and H. M. Mitchison. Splice-site mutations in the axonemal outer dynein arm docking complex gene ccdc114 cause primary ciliary dyskinesia. *Am J Hum Genet*, 92(1):88–98, 2013. ISSN 1537-6605 (Electronic) 0002-9297 (Linking). doi: 10.1016/j.ajhg.2012.11.002.
33. T. Kon, T. Oyama, R. Shimo-Kon, K. Imamula, T. Shima, K. Sutoh, and G. Kurisu. The 2.8 a crystal structure of the dynein motor domain. *Nature*, 484(7394):345–50, 2012. ISSN 1476-4687 (Electronic) 0028-0836 (Linking). doi: 10.1038/nature10955.
34. A. P. Carter, A. G. Diamant, and L. Urnavicius. How dynein and dynactin transport cargos: a structural perspective. *Current Opinion in Structural Biology*, 37:62–70, 2016. ISSN 0959-440x. doi: 10.1016/j.sbi.2015.12.003.
35. M. Ichikawa, D. Liu, P. L. Kastritis, K. Basu, T. C. Hsu, S. Yang, and K. H. Bui. Subnanometre-resolution structure of the doublet microtubule reveals new classes of microtubule-associated proteins. *Nat Commun*, 8:15035, 2017. ISSN 2041-1723 (Electronic) 2041-1723 (Linking). doi: 10.1038/ncomms15035.
36. William L. Dentler. *Chapter 3 Isolation of Cilia from Tetrahymena thermophila*, pages 13–15. Methods in Cell Biology. 1995. ISBN 9780125641487. doi: 10.1016/s0091-679x(08)60784-0.
37. T. M. Gibson and D. J. Asai. Isolation and characterization of 22s outer arm dynein from tetrahymena cilia. *Methods Cell Biol*, 62:433–40, 2000. ISSN 0091-679X (Print) 0091-679X (Linking). doi: 10.1016/s0091-679x(08)61547-2.
38. B. Kastner, N. Fischer, M. M. Golas, B. Sander, P. Dube, D. Boehringer, K. Hartmuth, J. Deckert, F. Hauer, E. Wolf, H. Uchtenhagen, H. Urlaub, F. Herzog, J. M. Peters, D. Poerschke, R. Luhrmann, and H. Stark. Grafix: sample preparation for single-particle electron cryomicroscopy. *Nat Methods*, 5(1):53–5, 2008. ISSN 1548-7105 (Electronic) 1548-7091 (Linking). doi: 10.1038/nmeth1139.
39. J. Alper, V. Geyer, V. Mukundan, and J. Howard. Reconstitution of flagellar sliding. *Methods Enzymol*, 524:343–69, 2013. ISSN 1557-7988 (Electronic) 0076-6879 (Linking). doi: 10.1016/B978-0-12-397945-2.00019-6.
40. C. Gell, V. Bormuth, G. J. Brouhard, D. N. Cohen, S. Diez, C. T. Friel, J. Helenius, B. Nitzsche, H. Petzold, J. Ribbe, E. Schaffer, J. H. Stear, A. Trushko, V. Varga, P. O. Widlund, M. Zanic, and J. Howard. Microtubule dynamics reconstituted in vitro and imaged by single-molecule fluorescence microscopy. *Microtubules, in Vitro*, 95:221–245, 2010. ISSN 0091-679x. doi: 10.1016/S0091-679x(10)95013-9.
41. M. Castoldi and A. V. Popova. Purification of brain tubulin through two cycles of polymerization-depolymerization in a high-molarity buffer. *Protein Expression and Purification*, 32(1):83–88, 2003. ISSN 1046-5928. doi: 10.1016/S1046-5928(03)00218-3.
42. M. Mahamdeh, S. Simmert, A. Luchniak, E. Schaffer, and J. Howard. Label-free high-speed wide-field imaging of single microtubules using interference reflection microscopy. *Journal of Microscopy*, 272(1):60–66, 2018. ISSN 0022-2720. doi: 10.1111/jmi.12744.
43. F. Ruhnow, D. Zwicker, and S. Diez. Tracking single particles and elongated filaments with nanometer precision. *Biophysical Journal*, 100(11):2820–2828, 2011. ISSN 0006-3495. doi: 10.1016/j.bpj.2011.04.023.
44. J. B. Alper, M. Tovar, and J. Howard. Displacement-weighted velocity analysis of gliding assays reveals that chlamydomonas axonemal dynein preferentially moves conspecific microtubules. *Biophysical Journal*, 104(9):1989–1998, 2013. ISSN 0006-3495. doi: 10.1016/j.bpj.2013.03.041.
45. D. N. Mastronarde. Automated electron microscope tomography using robust prediction of specimen movements. *J Struct Biol*, 152(1):36–51, 2005. ISSN 1047-8477 (Print) 1047-8477 (Linking). doi: 10.1016/j.jsb.2005.07.007.
46. S. Q. Zheng, E. Palovcak, J. P. Armache, K. A. Verba, Y. Cheng, and D. A. Agard. Motioncor2: anisotropic correction of beam-induced motion for improved cryo-electron microscopy. *Nat Methods*, 14(4):331–332, 2017. ISSN 1548-7105 (Electronic) 1548-7091 (Linking). doi: 10.1038/nmeth.4193.
47. J. R. Kremer, D. N. Mastronarde, and J. R. McIntosh. Computer visualization of three-dimensional image data using imod. *J Struct Biol*, 116(1):71–6, 1996. ISSN 1047-8477 (Print) 1047-8477 (Linking). doi: 10.1006/jsbi.1996.0013.
48. D. N. Mastronarde. Dual-axis tomography: an approach with alignment methods that preserve resolution. *J Struct Biol*, 120(3):343–52, 1997. ISSN 1047-8477 (Print) 1047-8477 (Linking). doi: 10.1006/jsbi.1997.3919.
49. D. Nicastro, C. Schwartz, J. Pierson, R. Gaudette, M. E. Porter, and J. R. McIntosh. The molecular architecture of axonemes revealed by cryoelectron tomography. *Science*, 313(5789):944–8, 2006. ISSN 1095-9203 (Electronic) 0036-8075 (Linking). doi: 10.1126/science.1128618.
50. K. Zhang. Gctf: Real-time ctf determination and correction. *J Struct Biol*, 193(1):1–12, 2016. ISSN 1095-8657 (Electronic) 1047-8477 (Linking). doi: 10.1016/j.jsb.2015.11.003.
51. J. Zivanov, T. Nakane, B. O. Forsberg, D. Kimanius, W. J. Hagen, E. Lindahl, and S. H. Scheres. New tools for automated high-resolution cryo-em structure determination in relion-3. *Elife*, 7, 2018. ISSN 2050-084X (Electronic) 2050-084X (Linking). doi: 10.7554/eLife.42166.
52. A. Punjani, J. L. Rubinstein, D. J. Fleet, and M. A. Brubaker. cryosparc: algorithms for rapid unsupervised cryo-em structure determination. *Nat Methods*, 14(3):290–296, 2017. ISSN 1548-7105 (Electronic) 1548-7091 (Linking). doi: 10.1038/nmeth.4169.
53. P. Emsley, B. Lohkamp, W. G. Scott, and K. Cowtan. Features and development of coot. *Acta Crystallogr D Biol Crystallogr*, 66(Pt 4):486–501, 2010. ISSN 1399-0047 (Electronic) 0907-4449 (Linking). doi: 10.1107/S0907444910007493.
54. G. N. Murshudov, P. Skubak, A. A. Lebedev, N. S. Pannu, R. A. Steiner, R. A. Nicholls, M. D. Winn, F. Long, and A. A. Vagin. Refmac5 for the refinement of macromolecular crystal structures. *Acta Crystallogr D Biol Crystallogr*, 67 (Pt 4):355–67, 2011. ISSN 1399-0047 (Electronic) 0907-4449 (Linking). doi: 10.1107/S0907444911001314.
55. Ali Punjani, Haowei Zhang, and David J. Fleet. Non-uniform refinement: Adaptive regularization improves single particle cryo-em reconstruction. *bioRxiv*, page 2019.12.15.877092, 2019. doi: 10.1101/2019.12.15.877092.
56. E. F. Pettersen, T. D. Goddard, C. C. Huang, G. S. Couch, D. M. Greenblatt, E. C. Meng, and T. E. Ferrin. Ucsf chimera–a visualization system for ex-

bioRxiv preprint doi: https://doi.org/10.1101/2020.12.08.415687; this version posted December 8, 2020. The copyright holder for this preprint (which was not certified by peer review) is the author/funder, who has granted bioRxiv a license to display the preprint in perpetuity. It is made available under aCC-BY-NC-ND 4.0 International license.

ploratory research and analysis. *J Comput Chem*, 25(13):1605–12, 2004. ISSN 0192-8651 (Print) 0192-8651 (Linking). doi: 10.1002/jcc.20084.

57. D. E. Wilkes, V. Rajagopalan, C. W. Chan, E. Kniazeva, A. E. Wiedeman, and D. J. Asai. Dynein light chain family in tetrahymena thermophila. *Cell Motil Cytoskeleton*, 64(2):82–96, 2007. ISSN 0886-1544 (Print) 0886-1544 (Linking). doi: 10.1002/cm.20165.
58. P. Emsley and K. Cowtan. Coot: model-building tools for molecular graphics. *Acta Crystallographica Section D-Structural Biology*, 60:2126–2132, 2004. ISSN 2059-7983. doi: 10.1107/S0907444904019158.
59. L. A. Kelley, S. Mezulis, C. M. Yates, M. N. Wass, and M. J. Sternberg. The phyre2 web portal for protein modeling, prediction and analysis. *Nat Protoc*, 10(6):845–58, 2015. ISSN 1750-2799 (Electronic) 1750-2799 (Linking). doi: 10.1038/nprot.2015.053.
60. T. D. Goddard, C. C. Huang, E. C. Meng, E. F. Pettersen, G. S. Couch, J. H. Morris, and T. E. Ferrin. Ucsf chimerax: Meeting modern challenges in visualization and analysis. *Protein Sci*, 27(1):14–25, 2018. ISSN 1469-896X (Electronic) 0961-8368 (Linking). doi: 10.1002/pro.3235.
61. J. Schindelin, I. Arganda-Carreras, E. Frise, V. Kaynig, M. Longair, T. Pietzsch, S. Preibisch, C. Rueden, S. Saalfeld, B. Schmid, J. Y. Tinevez, D. J. White, V. Hartenstein, K. Eliceiri, P. Tomancak, and A. Cardona. Fiji: an open-source platform for biological-image analysis. *Nat Methods*, 9(7):676–82, 2012. ISSN 1548-7105 (Electronic) 1548-7091 (Linking). doi: 10.1038/nmeth.2019.
62. G. Tang, L. Peng, P. R. Baldwin, D. S. Mann, W. Jiang, I. Rees, and S. J. Ludtke. Eman2: an extensible image processing suite for electron microscopy. *J Struct Biol*, 157(1):38–46, 2007. ISSN 1047-8477 (Print) 1047-8477 (Linking). doi: 10.1016/j.jsb.2006.05.009.
63. P. Gouet, E. Courcelle, D. I. Stuart, and F. Metoz. Espript: analysis of multiple sequence alignments in postscript. *Bioinformatics*, 15(4):305–8, 1999. ISSN 1367-4803 (Print) 1367-4803 (Linking). doi: 10.1093/bioinformatics/15.4.305.

bioRxiv preprint doi: https://doi.org/10.1101/2020.12.08.415687; this version posted December 8, 2020. The copyright holder for this preprint (which was not certified by peer review) is the author/funder, who has granted bioRxiv a license to display the preprint in perpetuity. It is made available under aCC-BY-NC-ND 4.0 International license.

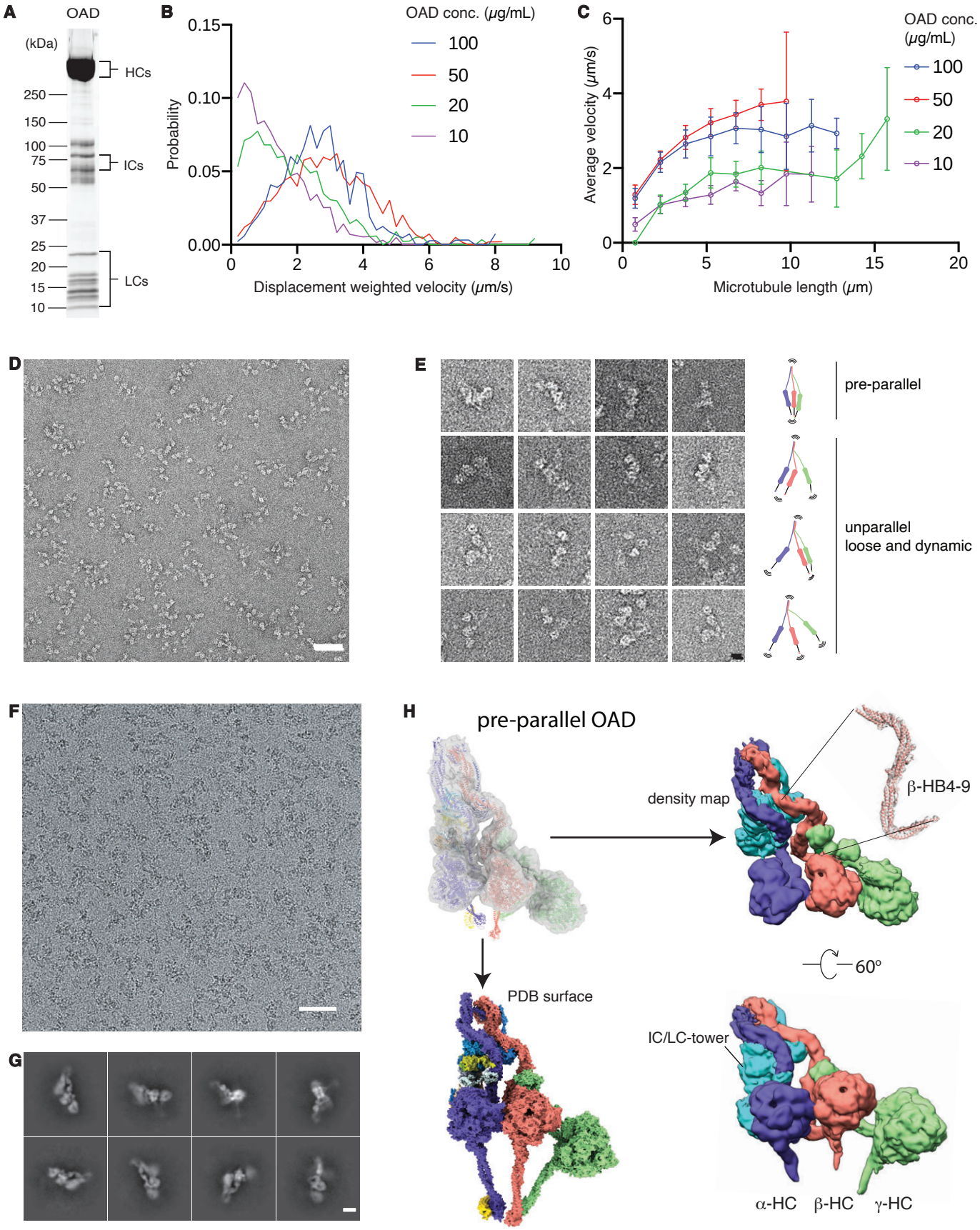

bioRxiv preprint doi: https://doi.org/10.1101/2020.12.08.415687; this version posted December 8, 2020. The copyright holder for this preprint (which was not certified by peer review) is the author/funder, who has granted bioRxiv a license to display the preprint in perpetuity. It is made available under aCC-BY-NC-ND 4.0 International license.

Fig. S1. Free OAD sample preparation and structure determination.
(A) SDS-PAGE of free OAD sample stained by SYPRO Ruby. **(B-C)** Microtubule gliding assay of the free OAD. **(D)** A representative micrograph of the free OAD sample by negative-stain electron microscopy (ns-EM). Scale bar, 100 nm. **(E)** Representative two-dimensional (2D) projection of the free OAD sample with a model attached for each row. The three motor domains and tail region have a wide range of dynamic conformations. Scale bar, 10 nm. **(F)** A representative cryo-EM micrograph of the free OAD sample after Grafix *(37)* purification (upper). Scale bar, 100 nm. **(G)** Representative 2D averages of the free OAD sample (lower). Scale bar, 10 nm. **(H)** The cryo-EM structure of pre-parallel OAD in two different views. The pre-parallel conformation is characterized by relative rotations among the three motors along with the stalks converging toward the MTBD region. The local density map of the β-HB4-9 is attached at upper right.

bioRxiv preprint doi: https://doi.org/10.1101/2020.12.08.415687; this version posted December 8, 2020. The copyright holder for this preprint (which was not certified by peer review) is the author/funder, who has granted bioRxiv a license to display the preprint in perpetuity. It is made available under aCC-BY-NC-ND 4.0 International license.

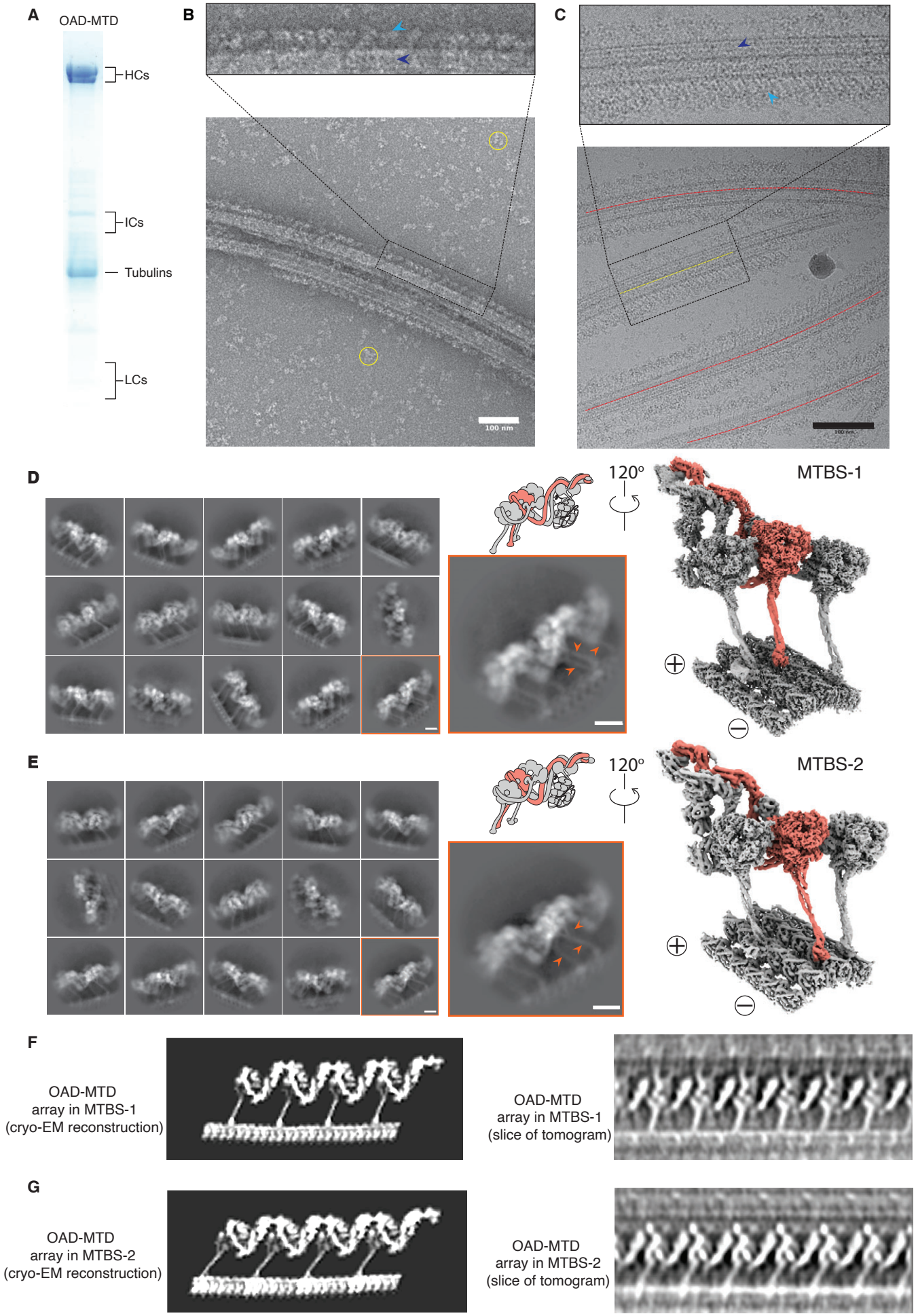

bioRxiv preprint doi: https://doi.org/10.1101/2020.12.08.415687; this version posted December 8, 2020. The copyright holder for this preprint (which was not certified by peer review) is the author/funder, who has granted bioRxiv a license to display the preprint in perpetuity. It is made available under aCC-BY-NC-ND 4.0 International license.

Fig. S2. The two microtubule-binding states of OAD-MTD array.

(A) SDS-PAGE of OAD-MTD sample stained by Page-Blue solution shows its multiple subunits. **(B)** A representative ns-EM micrograph of the reconstituted OAD-MTD sample shows that the highly ordered OAD arrays with 24-nm periodicity are formed in the absence of nucleotides and DC complex, in line with previous findings *(6, 60, 61)*. The OAD array and MTD are indicated by sky blue and blue arrows, respectively. The excessive free OADs are marked by yellow circles in the background (before centrifugation). Scale bar, 100 nm. **(C)** An example of the cryo-EM micrograph of the OAD-MTD sample. The OAD array and MTD are indicated by sky blue and blue arrows, respectively. The curved and nearly straight OAD-MTDs are indicated by red curves and a yellow line, respectively. Scale bar, 100 nm. **(D-E)** Representative 2D classes (left) and cryo-EM map of the OAD-MTD array in MTBS-1 **(D)** and MTBS-2 **(E)**. The arrows indicate differences of the stalk orientations in MTBS-1 and MTBS-2 (lower middle). **(F-G)** A comparison between the single particle cryo-EM reconstruction of the reconstituted OAD arrays (left) and the corresponding states from our cryo-ET analysis (right). The slices are focused on β-HC to show the key difference between MTBS-1 **(F)** and MTBS-2 **(G)**.

bioRxiv preprint doi: https://doi.org/10.1101/2020.12.08.415687; this version posted December 8, 2020. The copyright holder for this preprint (which was not certified by peer review) is the author/funder, who has granted bioRxiv a license to display the preprint in perpetuity. It is made available under aCC-BY-NC-ND 4.0 International license.

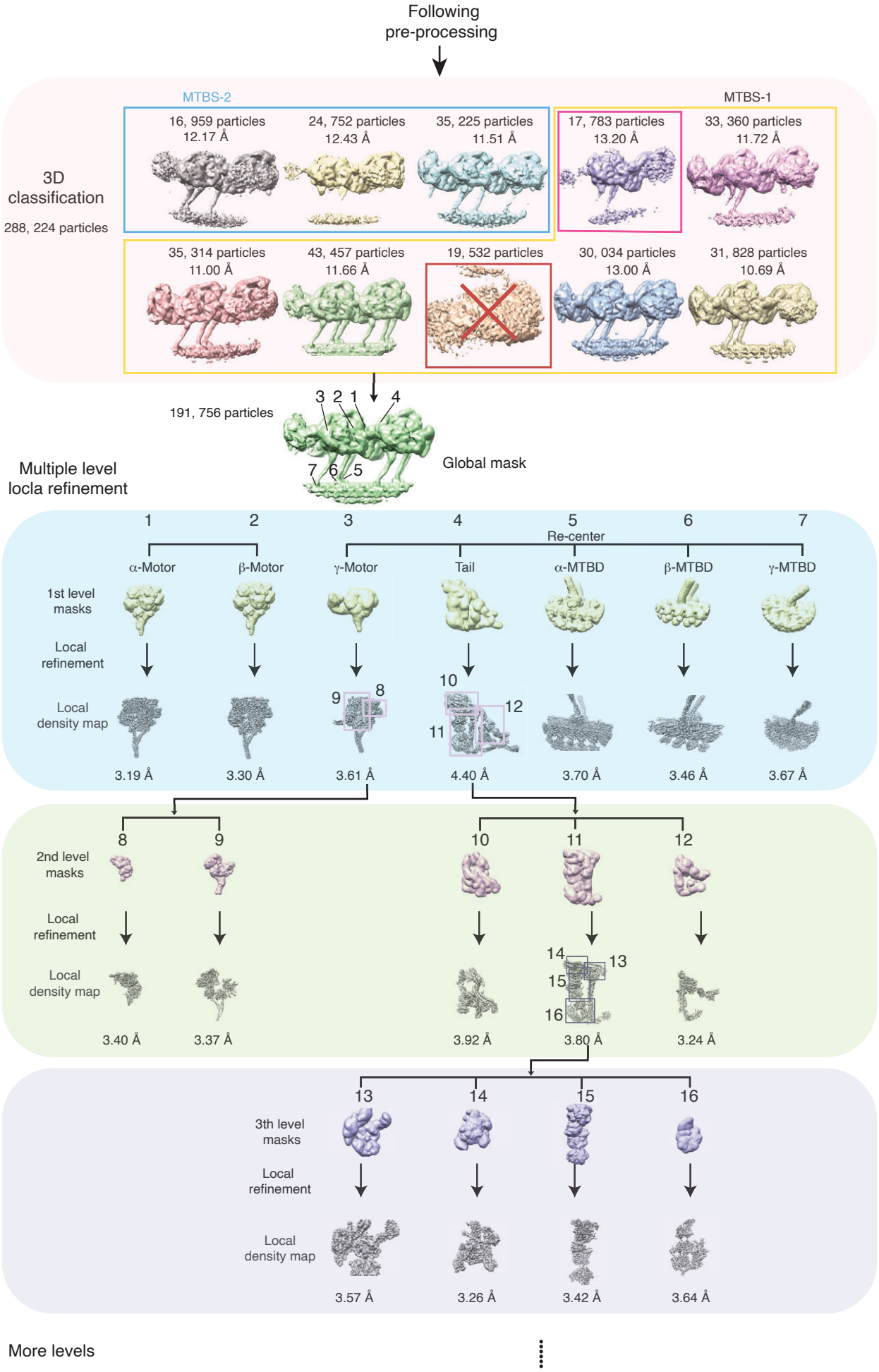

bioRxiv preprint doi: https://doi.org/10.1101/2020.12.08.415687; this version posted December 8, 2020. The copyright holder for this preprint (which was not certified by peer review) is the author/funder, who has granted bioRxiv a license to display the preprint in perpetuity. It is made available under aCC-BY-NC-ND 4.0 International license.

Fig. S3. Flow chart of the OAD structure determination.

The 3D classification identified two major microtubule-binding states (MTBS-1 and MTBS-2). The six good classes enclosed in the ginger rectangle are categorized into MTBS-1. The class composed of single OAD bond to the MTD (sOAD-MTD) in MTBS-1 was highlighted by a magenta square. The class in the red square was removed from the dataset for all following data processing. Three classes enclosed in sky blue rectangle are categorized into MTBS-2. Multiple levels of masks were implemented in the local refinement to improve the resolution of OAD-PF structure. The box size (~680 nm) was optimized to cover at least two adjacent OADs and the four PFs they bind to. The attached images represent typical local densities of the 3D volumes generated from cryoSPARC 2.12.

bioRxiv preprint doi: https://doi.org/10.1101/2020.12.08.415687; this version posted December 8, 2020. The copyright holder for this preprint (which was not certified by peer review) is the author/funder, who has granted bioRxiv a license to display the preprint in perpetuity. It is made available under aCC-BY-NC-ND 4.0 International license.

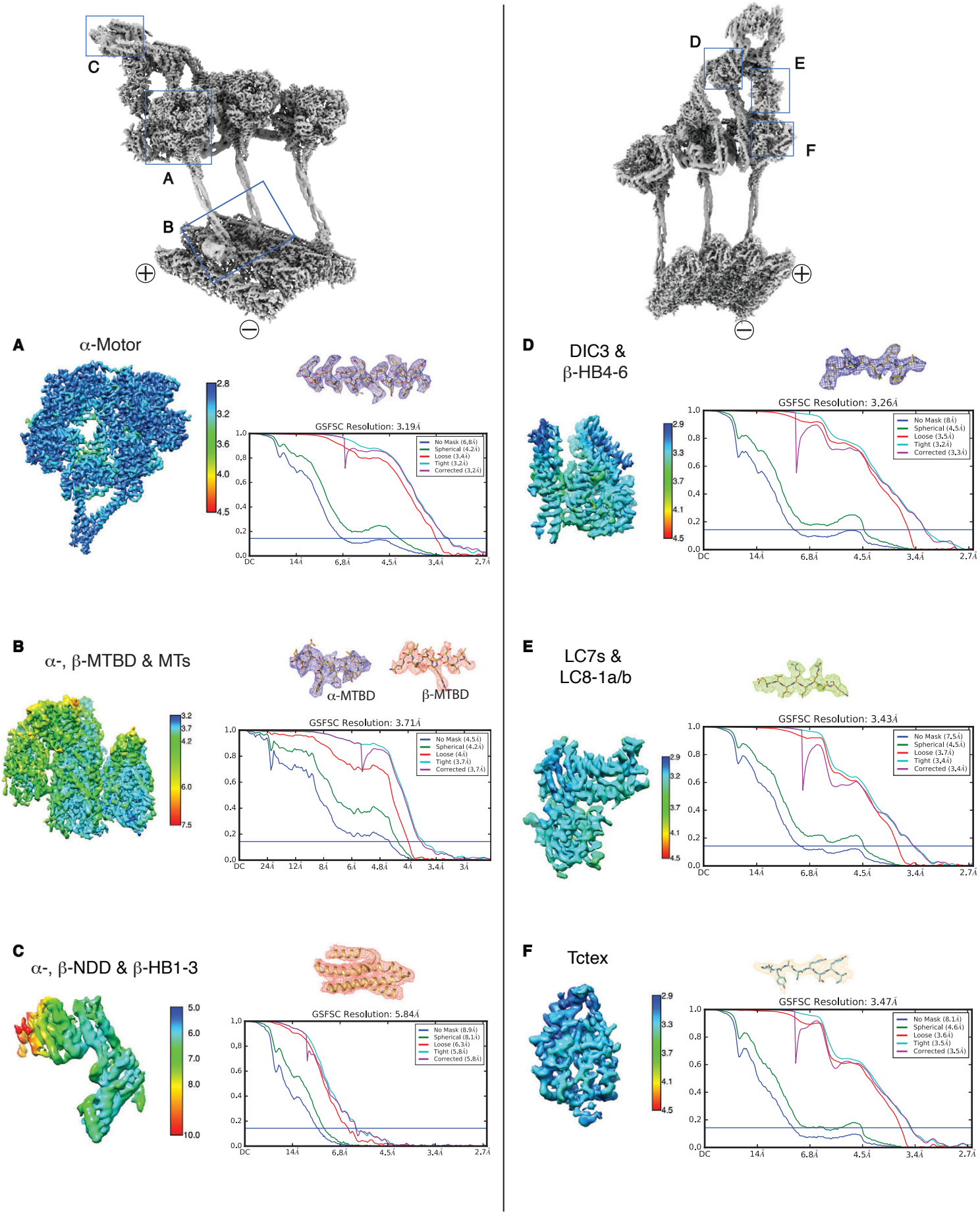

bioRxiv preprint doi: https://doi.org/10.1101/2020.12.08.415687; this version posted December 8, 2020. The copyright holder for this preprint (which was not certified by peer review) is the author/funder, who has granted bioRxiv a license to display the preprint in perpetuity. It is made available under aCC-BY-NC-ND 4.0 International license.

Fig. S4. Representative cryo-EM maps of the final local refinement.

Schematic of the representative masks used for local refinement from the distal (left) and proximal (right) view of the axoneme. To ensure the quality of the joint regions, a third mask is applied so that there is enough overlap in-between each two adjacent masks for OAD-PF structure determination. The local resolutions, FSC curves, and representative regions with the atomic model fitted into the local density for each mask from the distal view **(A-C)** and proximal view **(D-F)**.

bioRxiv preprint doi: https://doi.org/10.1101/2020.12.08.415687; this version posted December 8, 2020. The copyright holder for this preprint (which was not certified by peer review) is the author/funder, who has granted bioRxiv a license to display the preprint in perpetuity. It is made available under aCC-BY-NC-ND 4.0 International license.

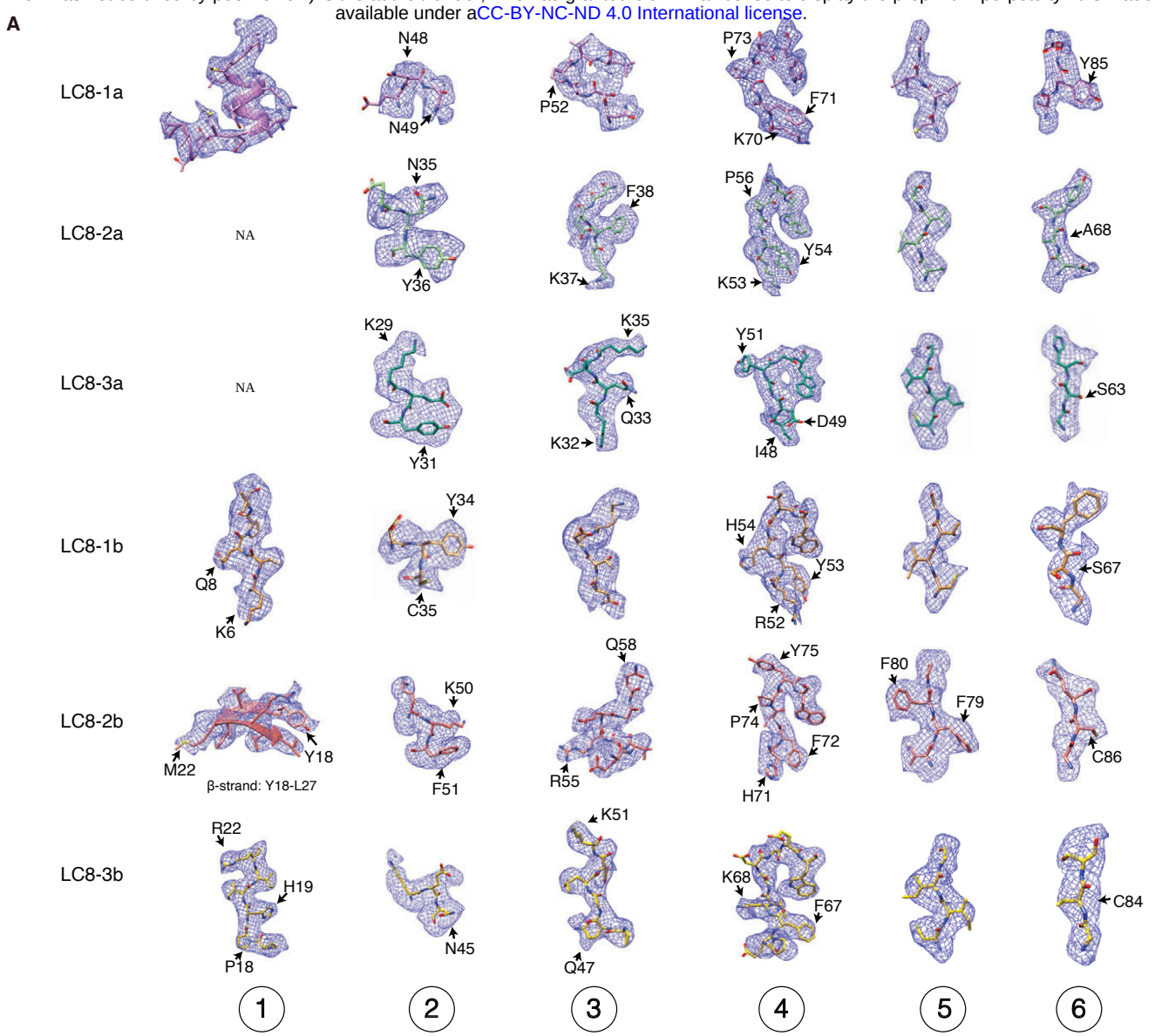

B

```
                                  1         10        20        30
LC8-1a (TTHERM_00716250)  MEQEKAVTDMDINELR..KLMIGKAIINSSDMQG..............DL
LC8-2a (TTHERM_00971840)  ......................MGDHANEQIIDMPE.........NSEMKSM
LC8-3a (TTHERM_01079060)  ......................MNHEPEVKATDMEE..............DM
LC8-1b (TTHERM_00449029)  ..............MS..HLDKVQPVIKNSDMSV..............EM
LC8-2b (TTHERM_00023950)  ............MASN..QQQKEDPKEQQQQYKTFMGARVLWPPECADDI
LC8-3b (TTHERM_000442909) ......MSDSDSDEGRVVEEPLPPHIIRFNDMAQ..............HL
LC8L1 (TTHERM_000649439)  ...............M..AQADRKAVIKNADMAE..............EM
LC8L2 (TTHERM_000463528)  ............MEIS..KEDKGKPVVKALDMTE..............EM
LC8L3 (TTHERM_000756449)  ..........MSKEPAQ..QSAGKKPTIKLADMPE..............DM
                                                                  1

                                  40        50        60        70
LC8-1a (TTHERM_00716250)  LQEAQDVIQSGIENNSAPVLNIEAACKYIKENLD.....KKFGPTWQCII
LC8-2a (TTHERM_00971840)  KNDAFSQAKFAVENY....KFENKISSHIKKFFD.....EKYGPNWHCVV
LC8-3a (TTHERM_01079060)  IKRVKEIAINAVKEY....KQEKQIAHYIKYEFD.....KIDGYGWNCIV
LC8-1b (TTHERM_00449029)  QKEVEEVAKKAIDYC....NTDKEIATFIKDDFR.....SRYHGTWHCIV
LC8-2b (TTHERM_00023950)  LEGAIRETQDALKKFEIA.REGQKIAEHLKKYMD.....DHFDPYWHVFF
LC8-3b (TTHERM_000442909) LKKVIRQADVLIKEN..PQGLEKDIALNLVKFVKSQPEFKIGDGEWQCII
LC8L1 (TTHERM_000649439)  SQDAIDCANQALEKF....NIEKDIAAFIKKEFD.....KKYNPTWHCIV
LC8L2 (TTHERM_000463528)  ENDAYEVAKKALEKF....SIEKDMAQYIKLEFD.....RLYSTSWHCIV
LC8L3 (TTHERM_000756449)  QQDAQSITLSAIEKY....TNERDIAYQIKREFE.....RKYLGNWHCVV
                                  2         3                   4         5

                          80        90        100       110
LC8-1a (TTHERM_00716250)  GEGYAYDVTVQNNTLLFMF..YNGNLAVLIFKS.
LC8-2a (TTHERM_00971840)  GKHFNAYVSYDSKNF.IFF..YEGQLAILLYRKG
LC8-3a (TTHERM_01079060)  GRNFGSHIIHQTKKY.IFF..KINELCLLLWKA.
LC8-1b (TTHERM_00449029)  GRNFGSFVTFERSYY.IYL..YVGQLAILLFKTG
LC8-2b (TTHERM_00023950)  GKNFGCQAVHNKNRF.IYF..YIEKTAFLMYQTQ
LC8-3b (TTHERM_000442909) GKNFGCSLTFDANVL.AFFDLLPSRKSILLFKSG
LC8L1 (TTHERM_000649439)  GRNFGSYVTHETKHF.IYF..YMGQVAILLFKSG
LC8L2 (TTHERM_000463528)  GKQFGSYVSHDSKHY.IYF..YIGEMSFLLYKFG
LC8L3 (TTHERM_000756449)  GKQFSSYVTHEEGYF.VQL..SKGPLQILLFRC.
                                  6
```

bioRxiv preprint doi: https://doi.org/10.1101/2020.12.08.415687; this version posted December 8, 2020. The copyright holder for this preprint (which was not certified by peer review) is the author/funder, who has granted bioRxiv a license to display the preprint in perpetuity. It is made available under aCC-BY-NC-ND 4.0 International license.

Fig. S5. The atomic resolution of cryo-EM density map distinguishes all six LC8s each other. **(A)** Despite their highly similar backbone structures, each of the six LC8-like proteins (LC8s) is clearly different from the others by its characteristic side chain densities and loops, which allowed us to distinguish them unambiguously. For example, a larger N-terminal α-helix in LC8-1a (LC10) and a special β strand in LC8-2b distinguish them from the others. Several representative residues for the identification are indicated by the black arrows. **(B)** Sequence alignment of the nine LC8s available in the Tetrahymena Genome Database *(http://ciliate.org)*. The six identified LC8s are named by the relative positions in OAD structure and the remaining three LC8s that are not present in our structure are named by LC8-Like1/2/3 (LC8L1, LC8L2, LC8L3). Identical (white letter in the red background), similar (red letter in the yellow background), and dissimilar residues. The green lines, green arrows, and red box indicate the selected regions in **(A)**.

bioRxiv preprint doi: https://doi.org/10.1101/2020.12.08.415687; this version posted December 8, 2020. The copyright holder for this preprint (which was not certified by peer review) is the author/funder, who has granted bioRxiv a license to display the preprint in perpetuity. It is made available under aCC-BY-NC-ND 4.0 International license.

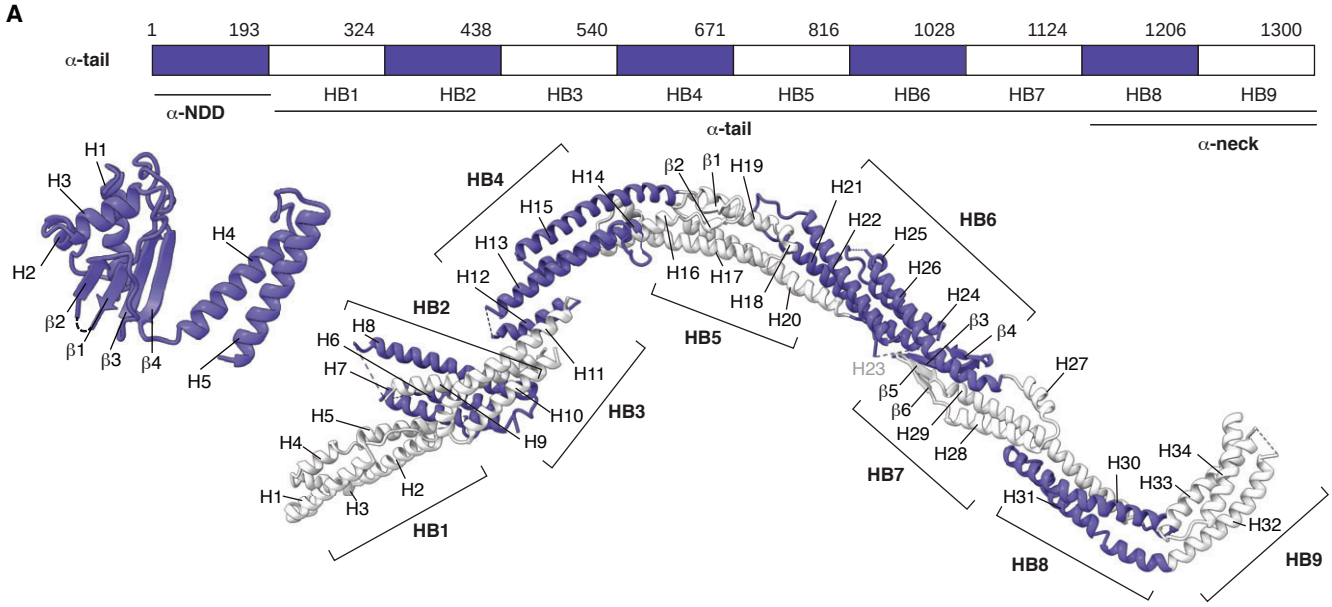

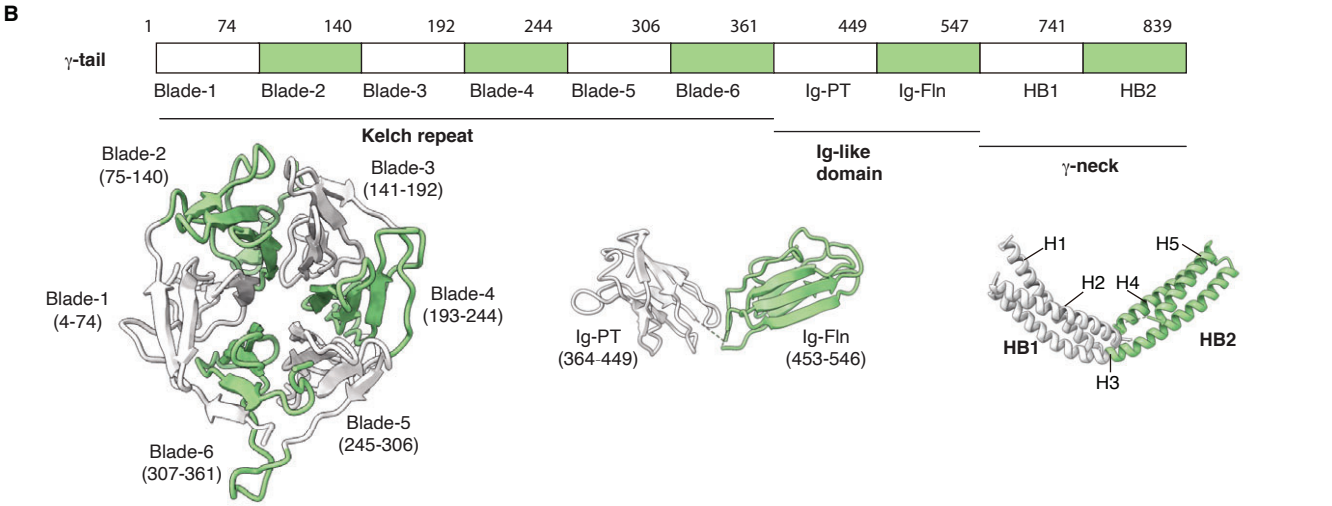

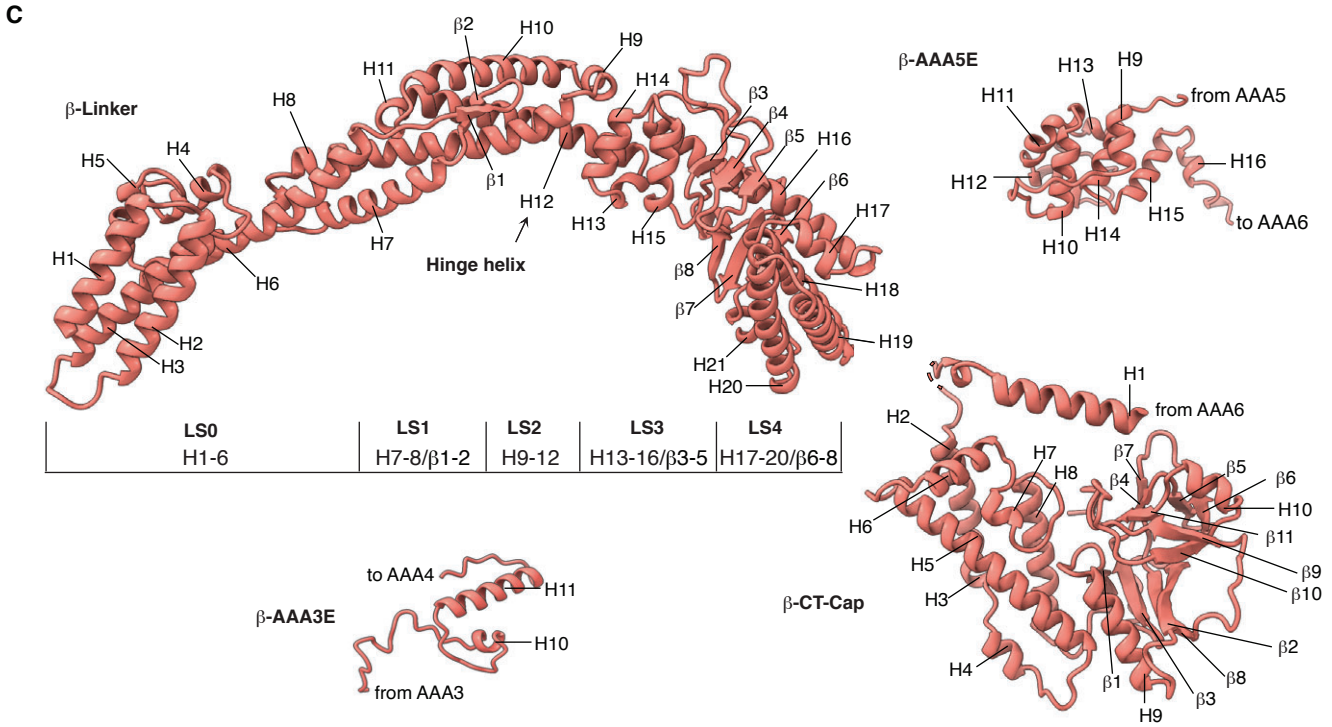

bioRxiv preprint doi: https://doi.org/10.1101/2020.12.08.415687; this version posted December 8, 2020. The copyright holder for this preprint (which was not certified by peer review) is the author/funder, who has granted bioRxiv a license to display the preprint in perpetuity. It is made available under aCC-BY-NC-ND 4.0 International license.

Fig. S6. Subdomain organization of the tail and Linker of OAD.

(A-B) Detailed index models of the subdomains of the tail region of α-HC **(A)** and γ-HC **(B)**. The subdomain of β-tail is the same as that of α-tail. **(C)** Detailed index models of the subdomains in the β-Linker region, motor domains AAA extensions (only the extensions used in this study are showed here), and CT-cap region. The subdomain of Linker and CT-cap of α-, γ-HC are the same as that of β-HC. The Linker helix H12 is the hinge helix *(31, 62, 63)* for the Linker and AAA+ ring swing. LS, Linker subdomain.

bioRxiv preprint doi: https://doi.org/10.1101/2020.12.08.415687; this version posted December 8, 2020. The copyright holder for this preprint (which was not certified by peer review) is the author/funder, who has granted bioRxiv a license to display the preprint in perpetuity. It is made available under aCC-BY-NC-ND 4.0 International license.

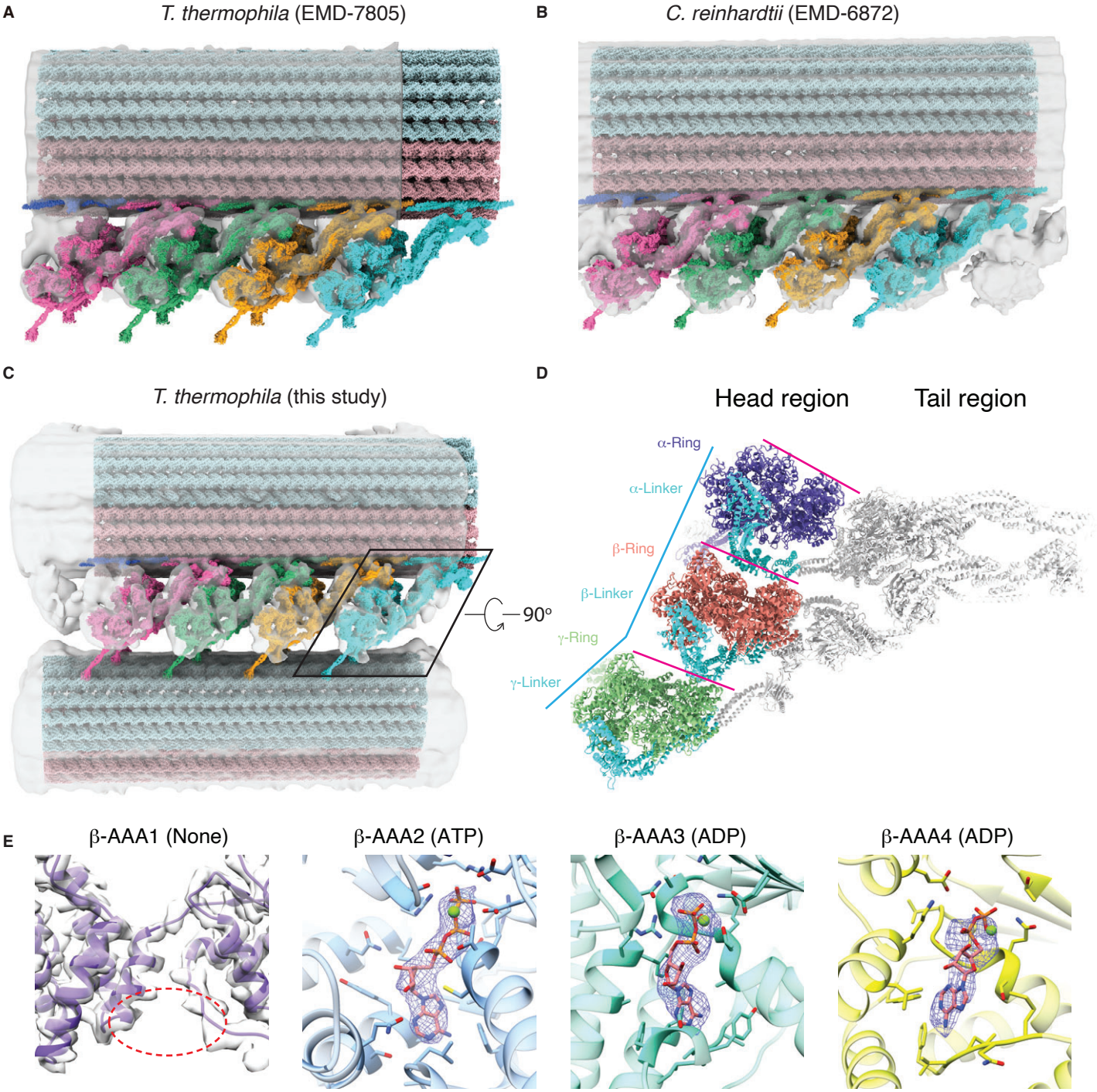

bioRxiv preprint doi: https://doi.org/10.1101/2020.12.08.415687; this version posted December 8, 2020. The copyright holder for this preprint (which was not certified by peer review) is the author/funder, who has granted bioRxiv a license to display the preprint in perpetuity. It is made available under aCC-BY-NC-ND 4.0 International license.

Fig. S7. A comparison between OAD array and cryo-ET structures in apo state.
(A-C) Rigid body fitting of our OAD array into cryo-ET maps of axonemes from *T. Thermophila* (EMD-7805) *(9)* **(A)**, *C. reinhardtii* (EMD-6872) *(10)* **(B)** and this study **(C)**. The four OAD units were fitted into the cryo-ET density en bloc rather than individually which verified the TTH interaction. The N-terminal regions of the tails are also close to DC and they are bridged by clear density connections. **(D)** Top view of the cryo-EM structure of OAD-PF unit shows that the three motor domains are organized in a nearly parallel architecture (the three pink lines). The relative positions of the α- and β-motor domains are aligned with the tubulin lattice. The center of the γ-motor domain is slightly ahead of the lattice line defined by connecting the centers of the other two (cyan polyline). The OAD appears as a triangle shape from top view, with the β- and γ-tail twisting toward the α-tail with respect to the motor domains. **(E)** Local densities of the nucleotides in AAA1-AAA4 of β-motor domain. Nucleotide density does not appear in β-AAA1. ATP in β-AAA2 and ADP in β-AAA3/AAA4 were unambiguously identified from the density. Other motor domains have the same nucleotide binding states.

bioRxiv preprint doi: https://doi.org/10.1101/2020.12.08.415687; this version posted December 8, 2020. The copyright holder for this preprint (which was not certified by peer review) is the author/funder, who has granted bioRxiv a license to display the preprint in perpetuity. It is made available under aCC-BY-NC-ND 4.0 International license.

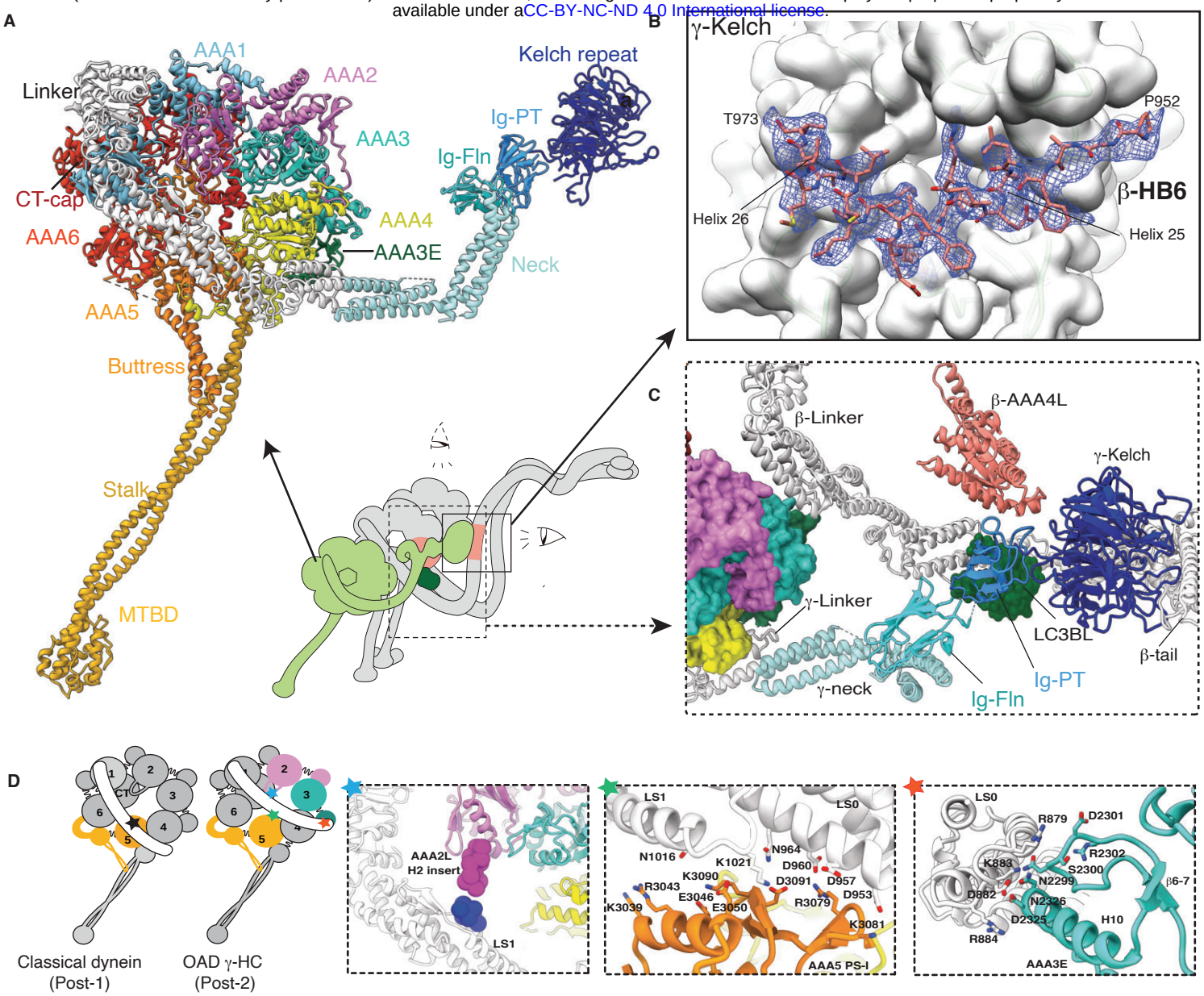

Fig. S8. The structure of γ-HC.

(A) The special architecture of γ-HC. **(B)** The γ-Kelch and β-tail are tightly bound together via a snug insertion of a 'V-shaped region' of β-tail into the γ-Kelch groove. **(C)** The γ-Ring is pinched between β- and γ-Linker. LC3BL resides at the joint region of β-Linker and β-neck. It links the β-Linker/neck region to γ-tail to form a local interaction network. **(D)** The novel γ-Linker docking mode (Post-2) which has three detailed Linker-Ring interaction sites indicated by colored pentagrams (blue, AAA2L H2-insert/LS1; green, AAA5 PS-I/LS0-1; and red, AAA3E/LS0).

bioRxiv preprint doi: https://doi.org/10.1101/2020.12.08.415687; this version posted December 8, 2020. The copyright holder for this preprint (which was not certified by peer review) is the author/funder, who has granted bioRxiv a license to display the preprint in perpetuity. It is made available under aCC-BY-NC-ND 4.0 International license.

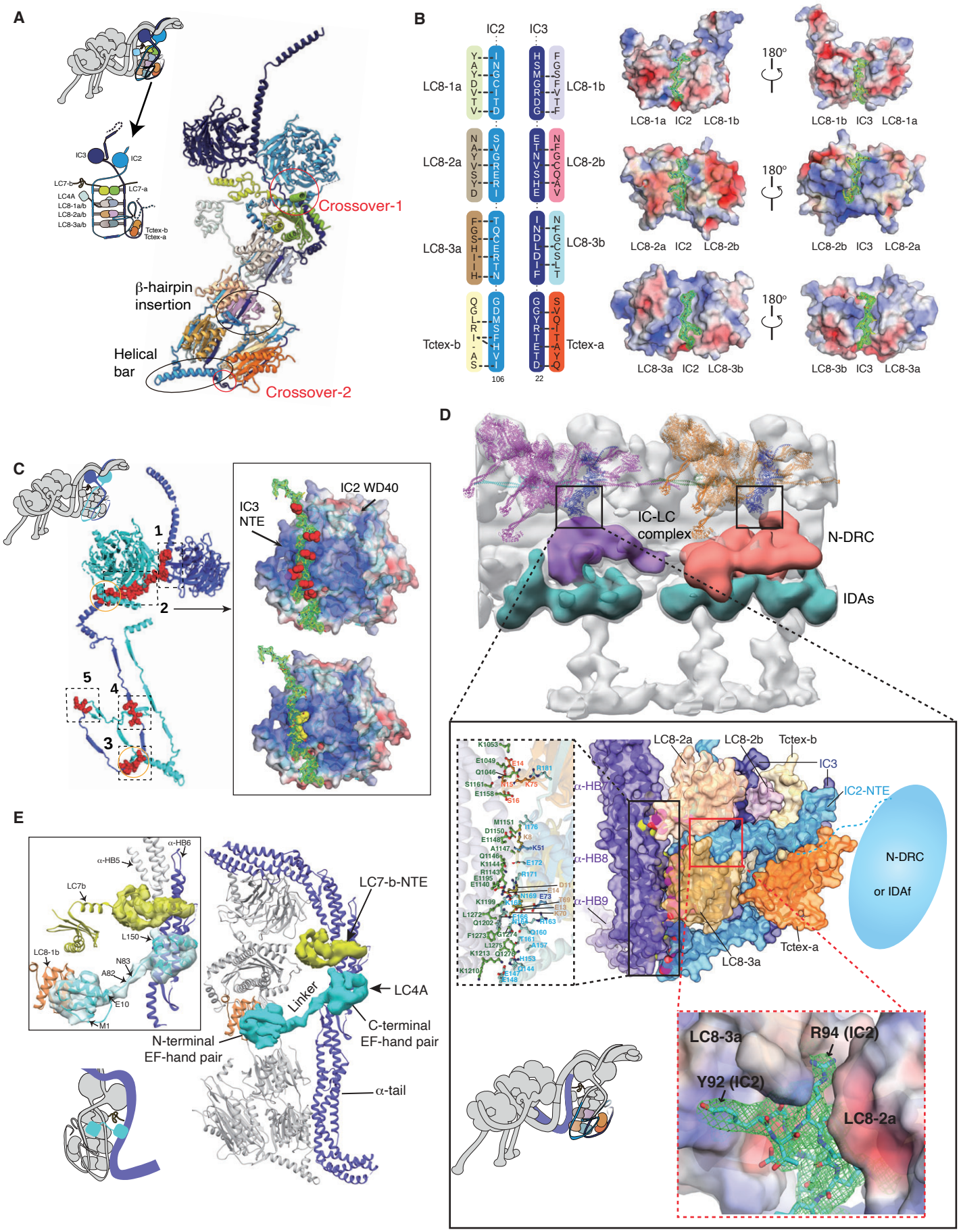

bioRxiv preprint doi: https://doi.org/10.1101/2020.12.08.415687; this version posted December 8, 2020. The copyright holder for this preprint (which was not certified by peer review) is the author/funder, who has granted bioRxiv a license to display the preprint in perpetuity. It is made available under aCC-BY-NC-ND 4.0 International license.

Fig. S9. The architecture of IC/LC-tower and its interaction with inner axonemal components.

(A) The IC/LC-tower of OAD, comprising five heterodimers, the LC7-a/b, LC8-1a/b, LC8-2a/b, LC8-3a/b and Tctex-a/b. In addition to the two crossovers and five contact sits between IC2/3 NTEs, a helical bar (residues N121-E147) and a beta-hairpin (residues N85-E100) of IC2 force the Tctex-a/b dimer to fold back and attach to the side of LC8-2a/b and LC8-3a/b, facing towards the inner side of the OAD array. The helical bar and beta-hairpin help stabilize the tower in such special organization, contrasting with dynein-1 and dynein-2 *(7, 64)*, in which the tower is linearly organized. **(B)** A schematic of the interaction interface between ICs and LCs (left) and the detailed interaction interfaces between IC2/3 and LC8s (right). **(C)** IC2 and IC3 interact with each other to form an assembly scaffold. The right panel shows the charge-charge interaction occurs between the positively charged groove (surface-charge rendering) of the IC2-WD40 domain and the negatively charged loop of IC3-NTE (residues Q125-N144), of which the negatively charged residues are shown as red sphere (upper right). In addition, two aromatic residues, Y132 and F133 (yellow sphere) of IC3-NTE insert into the small pits on the surface of IC2-WD40 (lower right). **(D)** The Tctex-a/b and IC2/3 NTEs of the IC/LC-tower are connected to the IC-LC complex of IADf (purple volume) and N-DRC (orange volume). The enlarged view of this linking region shows that the Tctex heterodimer is backfolded with a beta-hairpin of IC2-NTE specifically snug into the groove formed by LC8-2a/b and LC8-3a. The IC2-NTE (residues L61-W117), IC3-NTE (residues K12-K67), LC8-2a/b and LC8-3a/b, and Tctex-a/b formed the bottom region of the IC/LC-tower, tightly bind to α-neck. The close-up view of the closely packed interactions between bottom region of the IC/LC-tower and α-neck (left). The interacting residues are shown as sticks. The cyan dashed line indicates the untraced residues of the IC2. **(E)** A complete cartoon model of IC/LC-tower and α-tail, including the LC7-b-NTE and LC4A. The N-terminal EF-hand pair binds to HB6 of the α-tail, which agrees very well with the IQ binding site *(65)*. The C-terminal EF-hand pair interacts with LC8-1b.

bioRxiv preprint doi: https://doi.org/10.1101/2020.12.08.415687; this version posted December 8, 2020. The copyright holder for this preprint (which was not certified by peer review) is the author/funder, who has granted bioRxiv a license to display the preprint in perpetuity. It is made available under aCC-BY-NC-ND 4.0 International license.

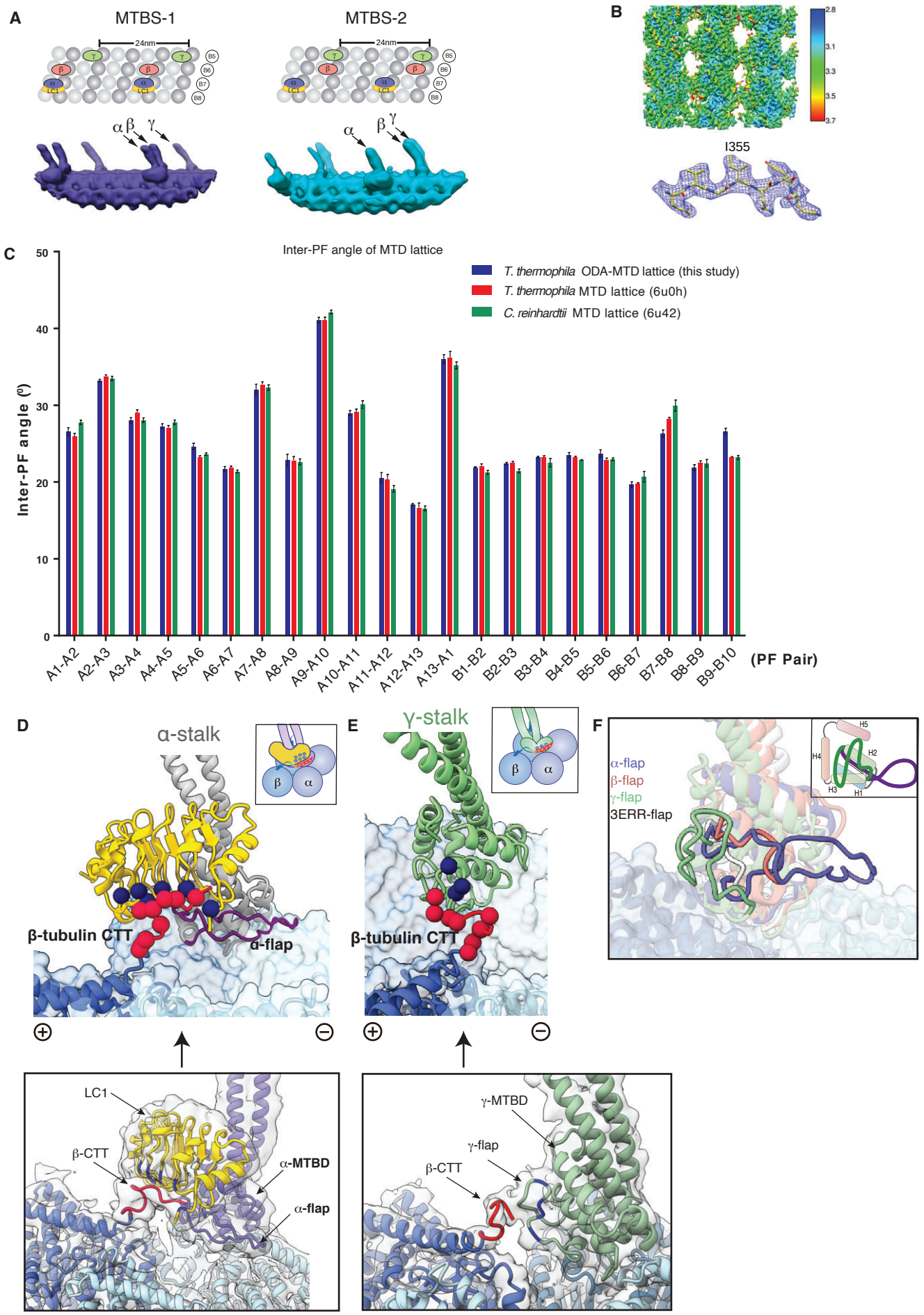

bioRxiv preprint doi: https://doi.org/10.1101/2020.12.08.415687; this version posted December 8, 2020. The copyright holder for this preprint (which was not certified by peer review) is the author/funder, who has granted bioRxiv a license to display the preprint in perpetuity. It is made available under aCC-BY-NC-ND 4.0 International license.

Fig. S10. The structures of OAD MTBDs and their interactions with microtubule doublet. **(A)** Synchronized positions of the OAD MTBDs bound to four microtubule protofilaments in MTBS1 and MTBS-2 (lower). The corresponding protofilaments of the native MTD are labeled in the attached model (upper). **(B)** The structure of MTD tubulins (16-nm repeat) locally refined to 3.08 Å resolution. **(C)** The inter-PF angles of the MTD lattice in this study shows the same pattern as previously published ones in both *T. thermophila* (PDB: 6u0h) *(23)* and *C. reinhardtii* (PDB: 6u42) *(24)*. **(D)** The negatively charged CTT (red sphere) of the adjacent β-tubulin is attracted to the positively charged (blue sphere) surface of LC1. The local density map of α-MTBD/LC1/tubulins was lowpass filtered to 6 Å to clearly show the density connection between β-CTT with LC1. **(E)** The interaction between γ-flap and β-CTT. The local density map was also lowpass filtered to 6 Å. **(F)** A comparison among the four flaps, including the three from our OAD structure and the low-affinity cytoplasmic dynein-1 MTBD (PDB: 3ERR, white) *(26)*. A cartoon model attaches at upper right.

bioRxiv preprint doi: https://doi.org/10.1101/2020.12.08.415687; this version posted December 8, 2020. The copyright holder for this preprint (which was not certified by peer review) is the author/funder, who has granted bioRxiv a license to display the preprint in perpetuity. It is made available under aCC-BY-NC-ND 4.0 International license.

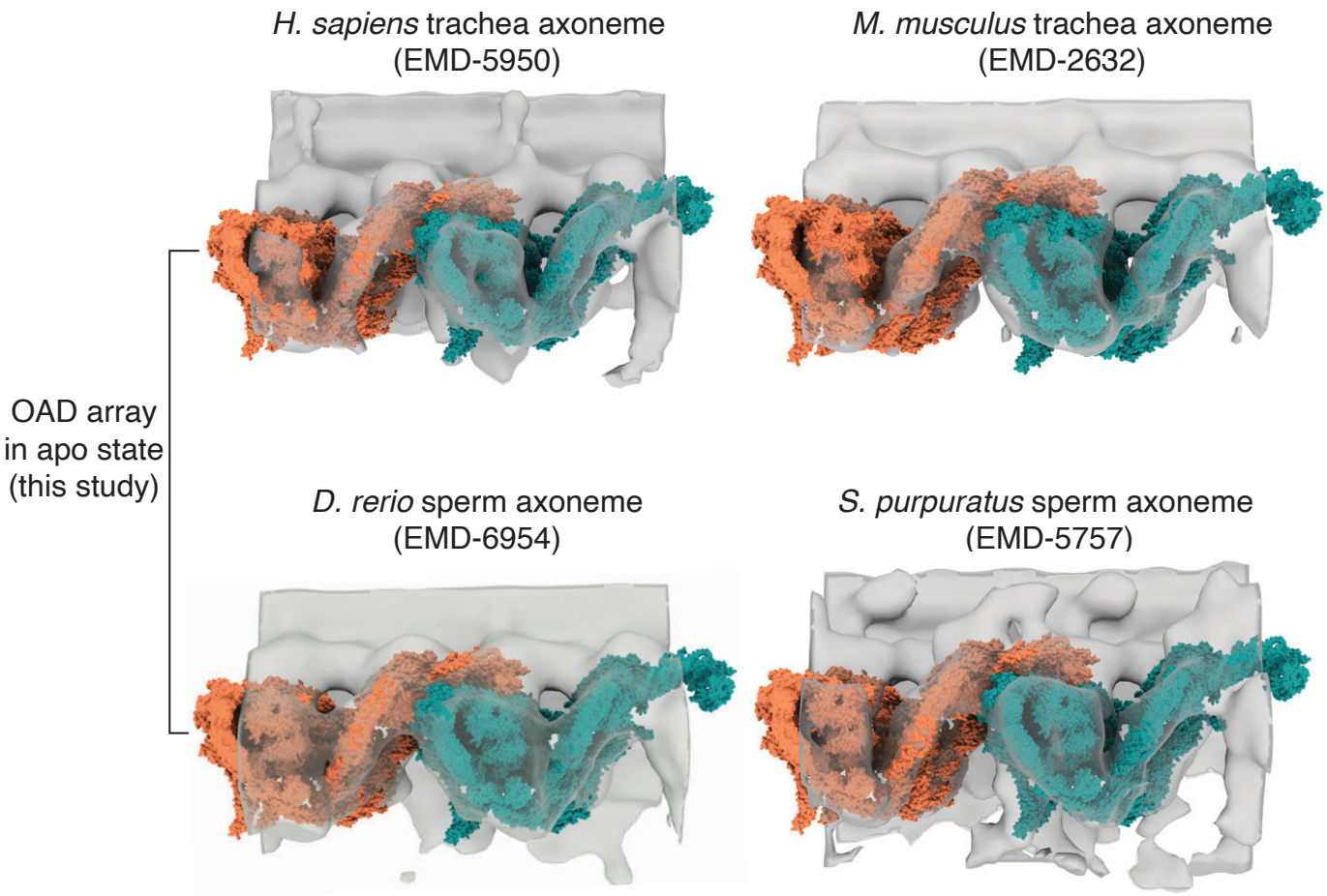

Fig. S11. The conserved TTH interactions in motile cilia across species.
The atomic model of our OAD array (γ-HC removed) fits well into previously reported cryo-ET maps of axoneme structures in apo state from four different organisms [human (*H. sapiens*), mouse (*M. musculus*), zebra fish (*D. rerio*), and sea urchin (*S. purpuratus*)], whose OAD contains two homologues of α- and β-heavy chains.

bioRxiv preprint doi: https://doi.org/10.1101/2020.12.08.415687; this version posted December 8, 2020. The copyright holder for this preprint (which was not certified by peer review) is the author/funder, who has granted bioRxiv a license to display the preprint in perpetuity. It is made available under aCC-BY-NC-ND 4.0 International license.

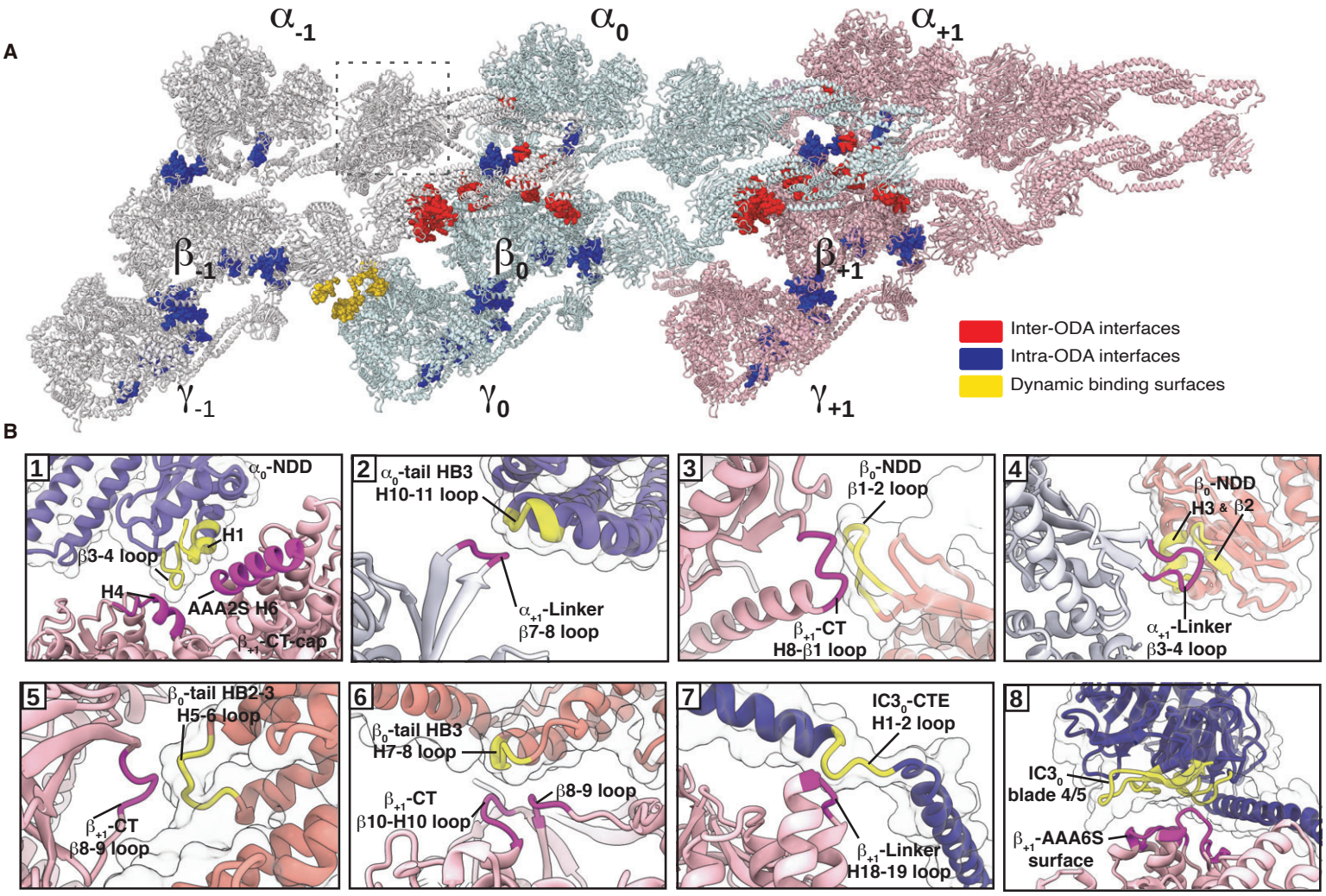

Fig. S12. The interaction network of OAD array.

(A) The top-view structure of the array networks formed by intra- (blue) and inter-ODA (red, yellow) interactions. **(B)** Enlarged views of the eight main interaction sites. The regions of OAD_0 and OAD_{+1} involved in interactions are marked in yellow and purple, respectively.

bioRxiv preprint doi: https://doi.org/10.1101/2020.12.08.415687; this version posted December 8, 2020. The copyright holder for this preprint (which was not certified by peer review) is the author/funder, who has granted bioRxiv a license to display the preprint in perpetuity. It is made available under aCC-BY-NC-ND 4.0 International license.

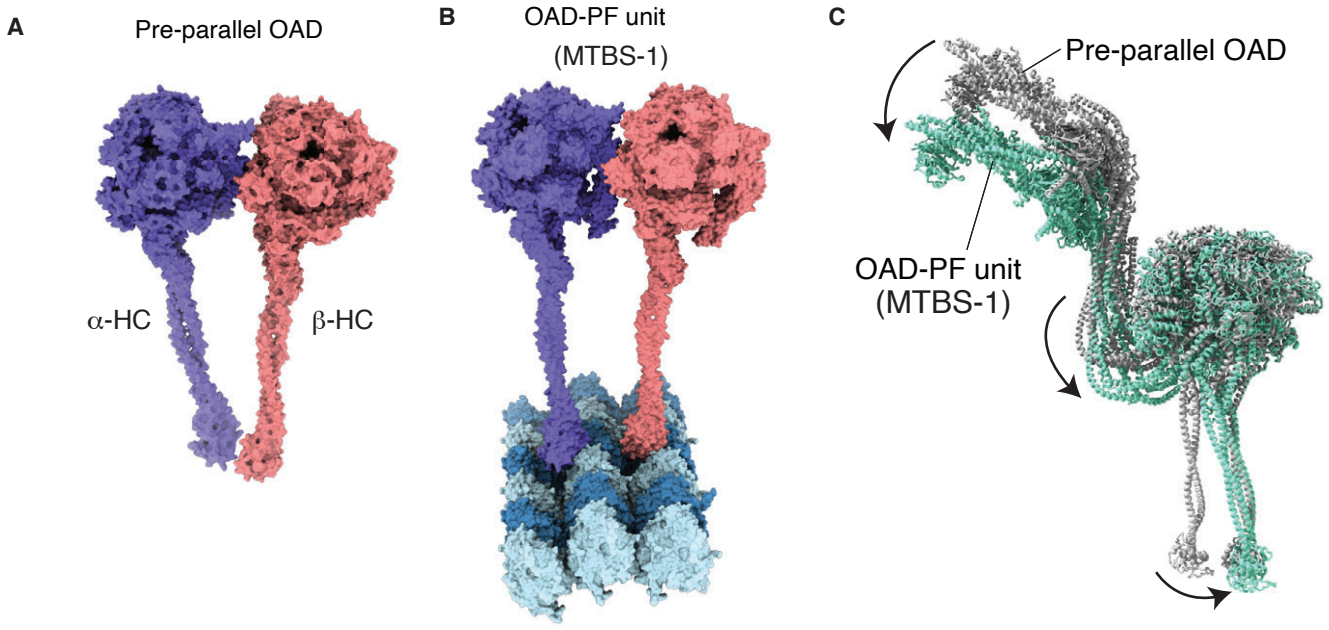

Fig. S13. A comparison between pre-parallel OAD and OAD array unit.
(A-B) Distal views of the pre-parallel OAD **(A)** and parallel OAD array unit **(B)**. **(C)** Side view of the global conformational changes from pre-parallel to parallel OAD. The two structures were superimposed by aligning their β-motor domains.

bioRxiv preprint doi: https://doi.org/10.1101/2020.12.08.415687; this version posted December 8, 2020. The copyright holder for this preprint (which was not certified by peer review) is the author/funder, who has granted bioRxiv a license to display the preprint in perpetuity. It is made available under aCC-BY-NC-ND 4.0 International license.

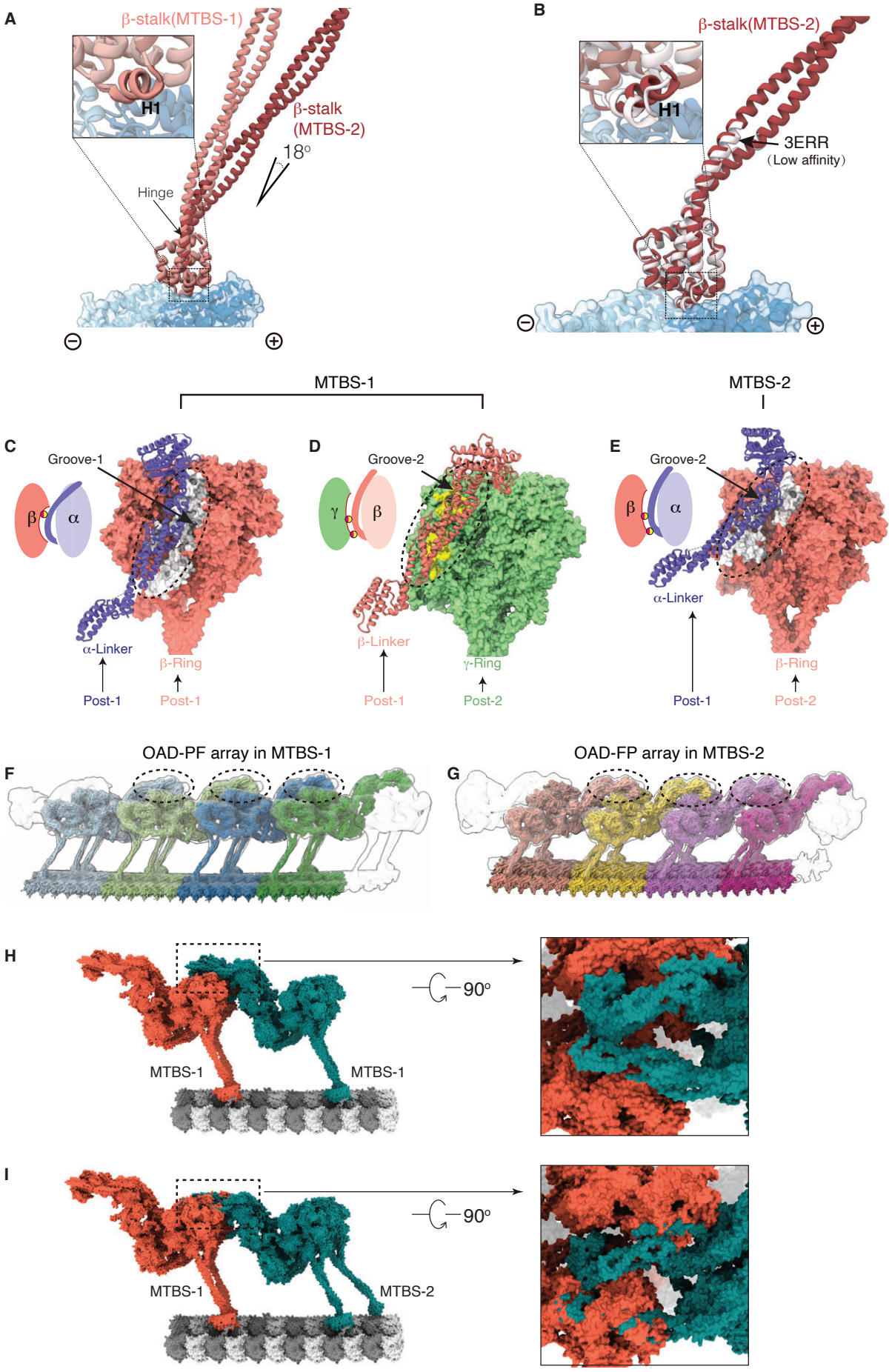

bioRxiv preprint doi: https://doi.org/10.1101/2020.12.08.415687; this version posted December 8, 2020. The copyright holder for this preprint (which was not certified by peer review) is the author/funder, who has granted bioRxiv a license to display the preprint in perpetuity. It is made available under aCC-BY-NC-ND 4.0 International license.

Fig. S14. A comparison between OAD-MTD arrays in MTBS-1 and MTBS-2.
(A) The β-MTBD in MTBS-2 adopts the same conformation as in MTBS-1 (upper left), while its stalk orients differently (18 degree). **(B)** The β-HC in MTBS-2 strikingly combines the low-affinity stalk conformation (black arrow) and the high-affinity MTBD H1 state (enlarged square at upper left). **(C-E)** The α-Linker moves its docking site on β-Ring from Groove-1 in MTBS-1 to Groove-2 in MTBS-2. **(F-G)** The OAD-MTD arrays in MTBS-1 and MTBS-2 are assembled in the same TTH manner. **(H-I)** Substituting one ODA unit in MTBS-1 with a unit in MTBS-2 severely disrupts the interactions between the IC-NDD_0 and the α/β_{+1}-LR region. The clashed region is highlighted in the black square.

bioRxiv preprint doi: https://doi.org/10.1101/2020.12.08.415687; this version posted December 8, 2020. The copyright holder for this preprint (which was not certified by peer review) is the author/funder, who has granted bioRxiv a license to display the preprint in perpetuity. It is made available under aCC-BY-NC-ND 4.0 International license.

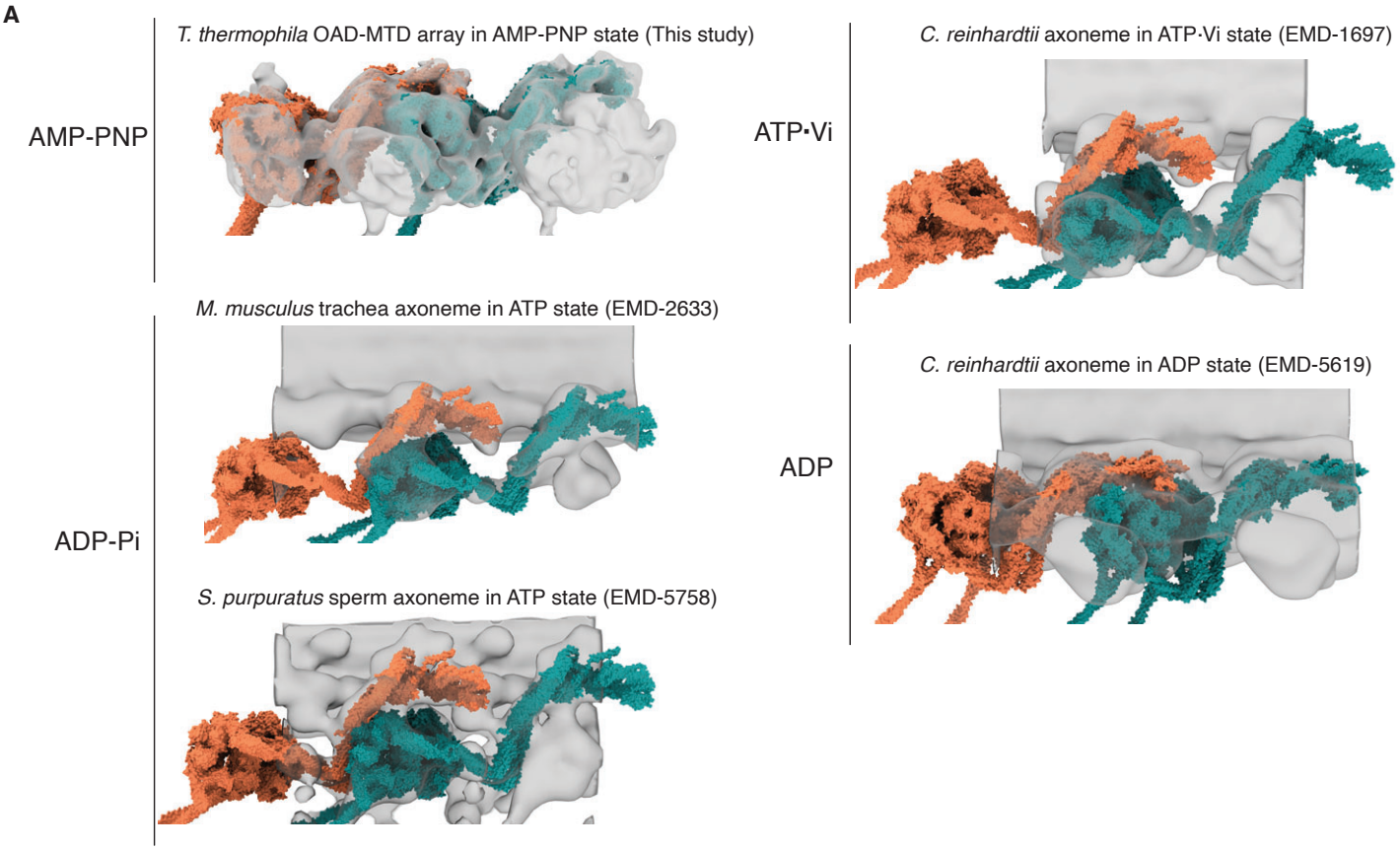

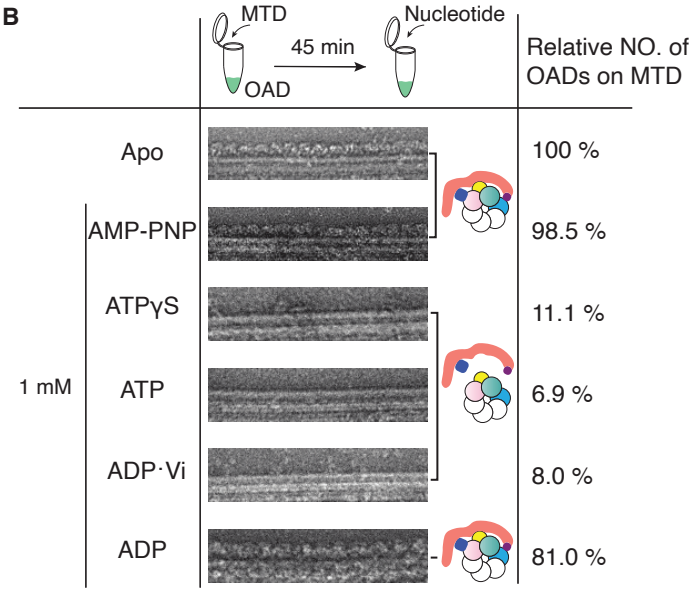

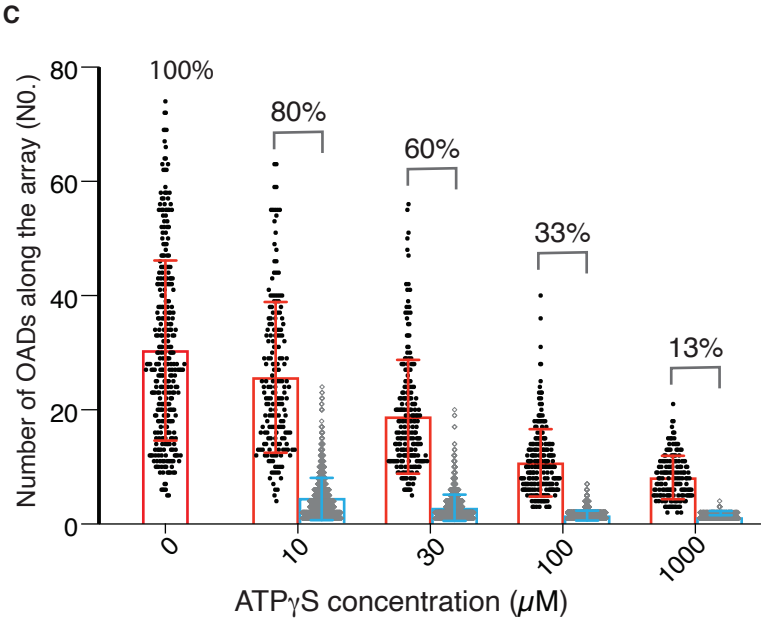

bioRxiv preprint doi: https://doi.org/10.1101/2020.12.08.415687; this version posted December 8, 2020. The copyright holder for this preprint (which was not certified by peer review) is the author/funder, who has granted bioRxiv a license to display the preprint in perpetuity. It is made available under aCC-BY-NC-ND 4.0 International license.

Fig. S15. The effects of different nucleotides on the TTH interactions of OAD arrays.
(A) Different conformations of OAD array during ATP cycle. The models (tomato and teal surfaces) were built based on previously reported cryo-ET maps (transparency grey) and our OAD coordinates. The TTH interactions in AMP-PNP and ADP states are similar to apo state. **(B)** The effects of different nucleotides on the reconstituted OAD-MTD arrays in vitro. ATPγS, ATP, and ADP.Vi disrupt almost all arrays, but AMP-PNP and ADP do not. The attached models show how different nucleotides affect the TTH inerfaces. Total OAD unit number of all arrays in the apo state was used as a reference and normalized as 100% for comparison. **(C)** The effect of ATPγS on the length of OAD array at different concentrations. Number of OADs on each continuous array was manually counted and showed as a single black dot at each condition. Percentage of top of each column represents the relative OAD coverage on MTDs (including individually bound OADs) at each ATPγS concentration compared to the apo state. Grey dots at each column represent computationally simulated distribution of the array lengths by stochastic disruption to the same coverage ratio as that of the experimental observation.

bioRxiv preprint doi: https://doi.org/10.1101/2020.12.08.415687; this version posted December 8, 2020. The copyright holder for this preprint (which was not certified by peer review) is the author/funder, who has granted bioRxiv a license to display the preprint in perpetuity. It is made available under aCC-BY-NC-ND 4.0 International license.

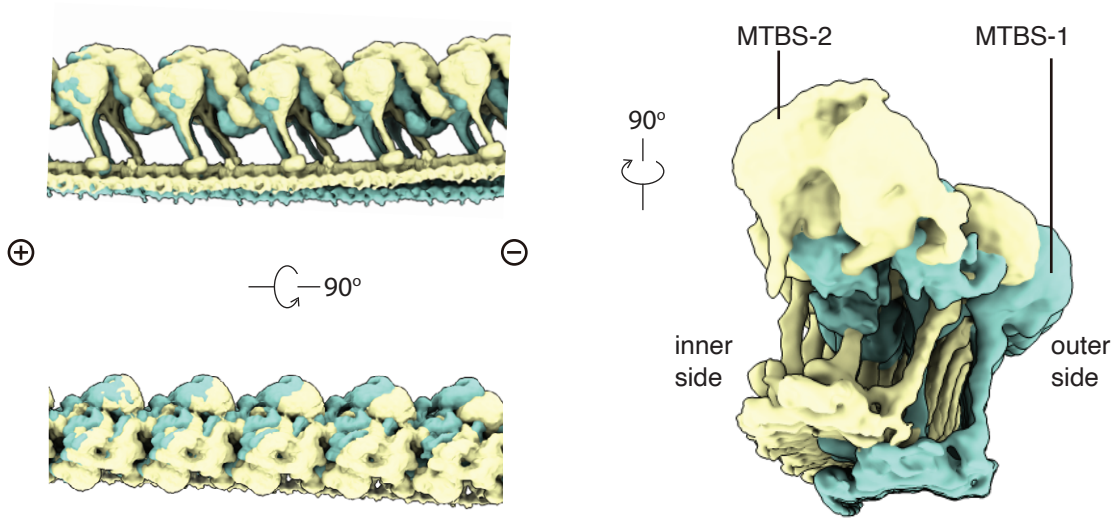

Fig. S16. A comparison between of OAD-MTD arrays in MTBS-1and MTBS-2.

bioRxiv preprint doi: https://doi.org/10.1101/2020.12.08.415687; this version posted December 8, 2020. The copyright holder for this preprint (which was not certified by peer review) is the author/funder, who has granted bioRxiv a license to display the preprint in perpetuity. It is made available under aCC-BY-NC-ND 4.0 International license.

Table S1. Cryo-EM data collection.

		OAD-MTD array (apo state)		**Free OAD (apo state)**	**OAD-MTD array (AMP-PNP)**
	Dataset 1	Dataset 2	Dataset 3	Dataset 1	Dataset 1
Microscope	Titan Krios	Titan Krios	Titan Krios	Titan Krios	Titan Krios
Voltage (kV)	300	300	300	300	300
Detector	K2	K2	K2	K2	K3
Frames	32	32	40	40	50
Exposure time (sec)	8	8	12	12	4
Total dose ($e^-/Å^2$)	53.3	53.3	53.3	53.3	41.56
Microscope sessions	1	3	3	1	1
Micrographs (No.)	1, 805	5, 689	4, 779	4, 847	1, 831
Defocus range (μm)	1.0 - 2.0	1.0 - 2.0	1.5 - 2.5	1.5 - 2.5	1.5 - 2.5
Energy filter slit (eV)	20	20	20	20	20
Pixel size (Å)	1.05	0.822	1.333	1.333	1.33
Final pixel size	1.333	1.333	1.333	2.666	3.99
Final box size	510	510	510	300	170
Final particles[#]	6, 895	72, 808	188, 989	36, 096	10, 796

bioRxiv preprint doi: https://doi.org/10.1101/2020.12.08.415687; this version posted December 8, 2020. The copyright holder for this preprint (which was not certified by peer review) is the author/funder, who has granted bioRxiv a license to display the preprint in perpetuity. It is made available under aCC-BY-NC-ND 4.0 International license.

Table S2. A summary of OAD subunits.

Subunit name (this paper)	Gene Model Identifier	TGD standard name	MW (KDa)	Uniprot ID	MS (significant matches)	Orthologues in *C.reinhardtii* (Uniprot ID)
α-HC	TTHERM_01276420	**DYH3**	534	Q22A67	1598	**γ-HC** (Q39575)
β-HC	TTHERM_00499300	**DYH4**	530	I7M9J2	1635	**β-HC** (Q39565)
γ-HC	TTHERM_00486600	**DYH5**	475	I7M6H4	1518	**α-HC** (Q39610)
IC2	TTHERM_00487150	**DIC2**	78	I7M008	280	**IC1** (Q39578)
IC3	TTHERM_00079230	**DIC3**	77	Q23FU1	397	**IC2** (P27766)
LC7-a	TTHERM_00348650	N/A	15	I7MHB1	72	**LC7a** (AAD45881)
LC7-b	TTHERM_00030210	**LC7B**	12	Q22MV2	73	**LC7b** (EDP03034)
LC8-1b	TTHERM_00716250	**LC10**	12	I7MCM8	25	**LC10** (EDP00562)
LC8-1a	TTHERM_00449029	**DLC82**	11	A4VE64	37	**LC8** (Q39580)
LC8-2b	TTHERM_00023950	N/A	12	Q22R86	29	
LC8-2a	TTHERM_00971840	**LC8E**	11	Q24DI9	15	
LC8-3b	TTHERM_000442909	N/A	13	W7XJB1	36	
LC8-3a	TTHERM_01079060	N/A	10	Q24CE5	39	
Tctex-a	TTHERM_00392979	N/A	13	A4VEB3	16	**LC9** (DAAZ95589)
Tctex-b	N/A	N/A	14	Q1HGH8	22	
LC3BL	TTHERM_00149859	N/A	13	A4VD75	44	**LC3** (Q39592)
LC1	TTHERM_00334290	**LC1**	22	I7M1N7	88	**LC1** (AAD41040)
LC4A	TTHERM_01075620	**LC4A**	18	Q22C78	21	**LC4** (Q39584)
α-tubulin	TTHERM_00558620	**ATU1**	49	I7M9N6	7	**TUA1** (Q540H1)
β-tubulin	TTHERM_00836580	**BTU2**	49	Q24B92	11	**TUB1** (A8IXZ0)

bioRxiv preprint doi: https://doi.org/10.1101/2020.12.08.415687; this version posted December 8, 2020. The copyright holder for this preprint (which was not certified by peer review) is the author/funder, who has granted bioRxiv a license to display the preprint in perpetuity. It is made available under aCC-BY-NC-ND 4.0 International license.

Table S3. Refinement summary of ODA-PF structures

3.1 ODA-PF in MTBS-1 (part-1)

Model composition	**α-motor domain**	**β-motor domain**	**γ-motor domain**	**IC2 (WD)**	**IC3 (WD)**	**LC7 & LC8-1**
Non-hydrogen atoms	21493	23197	21013	2923	2878	2791
Protein residues	2671	2688	2688	362	364	351
Ligands (GDP/GTP/Mg^{2+})	2/1/3	2/1/3	2/1/3			
Refinement statistics						
Resolution (Å)	3.19	3.30	3.38	3.57	3.26	3.80
R factor	0.3407	0.3388	0.3244	0.3536	0.3171	0.3630
Overall FSC	0.8011	0.7911	0.7575	0.6493	0.7879	0.7258
Correlation coefficient	0.9181	0.9367	0.9405	0.9257	0.9287	0.9002
Rms deviations						
Bond length (Å)	0.0025	0.0028	0.0029	0.0026	0.0040	0.0031
Bond angle (°)	1.2920	1.3220	0.3210	1.3392	1.3214	1.3428
Chiral volume ($Å^3$)	0.0449	0.0488	0.0481	0.0512	0.0461	0.0473
Validation						
Molprobity score	1.65 (100)	1.86(100)	1.77(100)	2.21(100)	2.01(100)	2.25(100)
Clashscore, all atoms	5.23(100)	5.02(100)	4.49(100)	7.04(100)	3.34(100)	5.37(100)
Good rotamers	90.17%	90.13%	91.41%	86.77%	89.03%	84.79%
Ramachandran plot						
Favored	97.10%	93.69%	94.65%	93.02%	90.06%	91.25%
Outliers	0.15%	0.49%	0.50%	0.84%	0.55%	0.58%
Cβ deviations > 0.25 Å	0.00%	0.00%	0.00%	0.00%	0.00%	0.00%

bioRxiv preprint doi: https://doi.org/10.1101/2020.12.08.415687; this version posted December 8, 2020. The copyright holder for this preprint (which was not certified by peer review) is the author/funder, who has granted bioRxiv a license to display the preprint in perpetuity. It is made available under aCC-BY-NC-ND 4.0 International license.

3.2 ODA-PF in MTBS-1 (part-2)

Model composition	**Kelch & β-HB5-7**	**α-MTBD /tubulins**	**β-MTBD /tubulins**	**γ-MTBD /tubulins**	**α-tail (HB4-8)**	**β-tail (HB3-5)**
Non-hydrogen atoms	4492	14625	14447	14515	4427	2245
Protein residues	600	1862	1844	1852	536	271
Ligands (GDP/GTP/Mg^{2+})	N/A	2/2/2	2/2/2	2/2/2	N/A	N/A
Refinement statistics						
Resolution	3.74	3.70	3.46	3.67	3.80	3.57
R factor	0.3650	0.3433	0.3320	0.3265	0.2599	0.3017
Overall FSC	0.7048	0.8058	0.8367	0.8075	0.7781	0.7382
Correlation coefficient	0.9150	0.8794	0.8636	0.8902	0.9848	0.9735
Rms deviations						
Bond length (Å)	0.0025	0.0034	0.0048	0.0032	0.0036	0.0040
Bond angle (°)	1.3300	1.3767	1.4032	1.3540	1.3819	1.2436
Chiral volume ($Å^3$)	0.0514	0.0515	0.0533	0.0496	0.0568	0.0506
Validation						
Molprobity score	2.28(99)	2.16(100)	2.10(100)	2.08(100)	1.95	2.08(100)
Clashscore, all atoms	5.26(100)	6.1(100)	4.84(100)	5.14(100)	3.82	9.75(97)
Good rotamers	86.39%	87.61%	87.36%	87.72%	88.26	92.46%
Ramachandran plot						
Favored	89.73%	91.66%	91.08%	90.68%	92.75	93.68%
Outliers	1.18%	0.54%	0.77%	0.76%	1.34	0.74%
Cβ deviations > 0.25 Å	0.00%	0.00%	0.00%	0.00%	0.19	0.00%

bioRxiv preprint doi: https://doi.org/10.1101/2020.12.08.415687; this version posted December 8, 2020. The copyright holder for this preprint (which was not certified by peer review) is the author/funder, who has granted bioRxiv a license to display the preprint in perpetuity. It is made available under aCC-BY-NC-ND 4.0 International license.

3.3 ODA-PF in MTBS-2

Model composition*	**α-motor domain**	**β-motor domain**	**γ-motor domain**
Non-hydrogen atoms	21493	21535	23540
Protein residues	2671	2661	2924
Ligands (GDP/GTP/Mg^{2+})	2/1/3	2/1/3	2/1/3
Refinement statistics			
Resolution	3.96	3.82	3.83
R factor	0.3063	0.3517	0.3469
Overall FSC	0.8486	0.8143	0.8240
Correlation coefficient	0.9050	0.9104	0.9144
Rms deviations			
Bond length (Å)	0.0031	0.0027	0.0027
Bond angle (°)	1.3286	1.2985	1.3010
Chiral volume ($Å^3$)	0.0496	0.0447	0.0456
Validation			
Molprobity score	1.90(100)	1.87(100)	1.71(100)
Clashscore, all atoms	4.56(100)	4.75(100)	3.92(100)
Good rotamers	88.26%	88.95%	91.75%
Ramachandran plot			
Favored	94.51%	95.54%	94.09%
Outliers	0.41%	0.26%	0.55%
Cβ deviations > 0.25 Å	0.00%	0.00%	0.00%

* All other regions in MTBS-2 were generated by rigid-body fitting of the corresponding coordinates from MTBS-1 and were not further refined.